理學碩士 學位論文

화합물 반도체내의 불균일성의 영향에 대한 연구

Study on the disorder effects of compound semiconductors

指導敎授 張 志 豪

2006 年 2 月

韓國海洋大學校 大學院

半導體物理轉攻

朴 昇 煥

本 論文을 朴昇煥의 理學碩士 學位論文으로 認准함

위원장 梁 珦 (인)

위 원 金 泓 承 (인)

위 원 張 志 豪 (인)

2006 년 2 월

한국해양대학교 대학원

Contents

국 문 요 약

본 논문에서는 반도체 내의 여러 가지 불균일성과 그 원인들을 광학적, 구조적, 전기적인 특성의 관점에서 고찰하였으며, 이 논문의 목적은 불균일성의 평가를 통해 반도체내의 불균일성을 조절하고 최소화 시킴으로써 반도체 소자의 성능을 이론 치에 가깝게 향상시키는데 기여함에 있다. 본 논문은 총 7장으로 구성 되어 있으며 각 장의 내용은 다음과 같다.

제 1 장에서는 세가지 원인으로부터 형성되는 반도체 내 여러 가지 불균일성과 이러한 불균일성에 대한 평가의 중요성에 대하여 설명하였다. 제 2 장에서는 불균일성을 평가하기 위해 본 연구에서 사용한 세가지 방법, PL, HRXRD 그리고 Hall 효과 측정에 대하여 소개하였다. 제 3 장에서는 $Zn_{1-x}Cd_xSe$ 양자우물의 불균일성을 PL 반치폭의 관점에서 소개하였다. 혼합물 불균일성과 계면 불균일성과 관계된 이론적 모델로부터 계산된 결과가 측정값과 상당한 일치를 가지고 있음을 알 수 있었다. 하지만, 양자우물 내 Cd 함량이 증가함에 따라 우물 내 Cd 내부 확산이 PL 반치폭의 또 다른 증가의 원인으로 작용함을 알아 내었다. 제 4 장에서는 $Zn_{1-x}Cd_xTe$ 양자우물의 혼합물 불균일성과 계면 불균일성을 PL 반치폭의 관점에서 소개하였다. 비록 반도체 내의 불균일성은 결정성장을 통하여 최소화 되었지만, 엑시톤 파동 함수의 확산이 반치폭을 증가시키는 또 다른 원인으로 작용함을 알아 내었다. 제 5 장에서는 후막 GaN의 구조적 특성을 HRXRD 측정을 통해서 조사하였다. Mosaicity, tilt, twist 그리고 bowing 과 같은 구조적 불균일성이 X-ray rocking curve를 통해 평가되었다. 또한 polishing에 의한 표면 damage층을 에칭 전, 후 PL 측정을 통해서 확인하

였고, 화학적 에칭을 통하여 얇은 표면 damage층을 제거하였다. 결과적으로 반도체 내의 불균일성과 결함 발생의 상호 관계에 대해서 명확히 할 수 있었다. 제 6 장에서는 AlN 버퍼층을 이용하여 성장시킨 GaN 박막의 전기적 특성이 온도변화 Hall 효과 측정을 통해서 확인되었다. 또한 포텐셜 장벽 모델을 이용하여 결함, 전위등에 의해 형성된 반도체 내 불균일성이 전자의 이동에 영향을 준다는 사실을 확인하였다. 제 7 장에서는 본 논문에서 얻은 결과를 정리하여 얻어진 결론을 기술하였다.

Abstract

In this paper, it has been investigated that 1) how to estimate several types of disorders, 2) What is the origins of disorders. It has been discussed in terms of optical, electrical, and structural properties. The purpose of this thesis is to control and reduce the disorders in semiconductors to improve the semiconductor device performance up to theoretical limits.

In the chapter 1, several types of disorders occurred due to three origins are introduced and the importance of the evaluation of those disorders is explained. In the chapter 2, the principles of photoluminescence spectroscopy, high resolution X-ray diffraction and Hall effects measurement are explained. In the chapter 3, $Zn_{1-x}Cd_xSe$ triple quantum wells are investigated. The PL linewidth broadening is analyzed from the point of the disorder induced inhomogeneous broadening. The calculated results from theoretical models related to composition and interface disorder strongly corresponding to experimental values. However, it was found that in the case of high Cd-content alloys the Cd inter-diffusion acts as an additional origin for PL linewidth broadening. In the chapter 4, $Zn_{1-x}Cd_xTe$ multi quantum wells are investigated in terms of PL linewidth broadening due to interface and composition broadening. The results indicate that although disorder can be minimized by the optimization of growth conditions, in a QW with very thin QW thickness, disclose of an exciton wave function will make an additional PL linewidth broadening. In the chapter 5, the structural qualities of GaN films are investigated using HRXRD measurement. Structural disorders including mosaicity,

tilt, twist and bowing are evaluated using X-ray rocking curve. Also, the surface-damage layers induced from structural disorder is removes by chemical etching. From these results, it is found that the structural disorders can be an origin of structural defects. In the chapter 6, electrical properties of GaN film grown on AlN buffer is investigated using temperature-dependent Hall effect measurement. The results indicate that the defects originated from disorders have a large influence on the electrical transportation of semiconductors. In the chapter 7, based on the results obtained from this thesis are summarized and concluded.

Chapter 1. Introduction

1.1) Introduction to disordered semiconductor

The theory of crystalline solids has been extremely successful in describing the bulk properties of most solids whose atoms are arranged on a periodic lattice. In fact, some properties such as electrical conductivity can be explained in some detail with no reference to a periodic lattice than that necessary to count quantum states.

However, all real semiconductors are disordered. Real semiconductors are grown at finite temperature, which produces defects thermodynamically. There exist many disorder effects in real semiconductor that may disturb an ideal crystalline order. The substitutional and interstitial defects, lattice displacements of static origin as well as those due to thermal vibrations, voids, precipitates, surfaces and grain boundaries typically exist in solids [1]. Even if, we imagine a perfect elemental semiconductor with no defects or impurities, there will be disorders due to the presence of more than one isotope.

1.2) Theoretical background

1.2.1) The general disorders in semiconductor

In general, the ordered state in the semiconductor is defined as the crystalline quality with infinitely repeated crystalline structure in three dimensional spaces. The translational symmetry of the crystal structure is the ordering rule. From the

position of one atom and the knowledge of the crystal structure, all atomic positions can be derived. However, it is clear that this is not the case of all structures. If there exist some randomness in the atomic positions, then it is impossible to predict the positions from an ordering rule.

Many practical applications use materials that are weakly or strongly disordered in detail. For example, the doping of semiconductors, which is absolutely necessary for electronic devices, can be viewed as a departure from perfect crystallinity. Hence a deeper understanding of the properties of disordered materials is desired in various technological applications. At the same time, effects of disorder are studied intensively from the viewpoint of fundamental physics. Many of the challenging problems within solid state physics today are connected to disorders.

Weak disorder may be defined as a perturbation of the perfect crystalline order. Defects, vacancies and dislocation belong to this category, which are frequently observed in real materials. In polycrystalline materials, the grain boundaries are more disordered configuration of atoms than the grains. Strong disorder signifies a marked departure from crystalline order. The basic property of amorphous materials is that they do not posses translational order with any long range. There exists an element of randomness in the atomic positions. The length scales which order of disorder persists are also on interest. As we will see many materials possess a local order over length scales of a few atoms or molecules, but are disordered on larger length scales. Inhomogeneous materials, such as 1multiphase

materials, composites and porous materials can be regarded as homogeneous on sufficiently large length scales, but the inhomogeneities lead to strong disorder on mesoscopic (nm-μm) length scales.

1.2.2) The origin of disorder

Real materials are never pure systems. The substrate itself will not be pure and thus will provide a certain amount of randomness to the system [2]. The occurrence of disorder structures can be seen as the outcome of the difference between physical laws and randomness.

Actually, three origins for the disorder occurrence can be considered, which are material properties mismatch, epitaxial growth and intrinsic problem. During the epitaxial growth, there exists several difference of material property such as lattice mismatch, thermal coefficient mismatch, crystallographic mismatch, heterovalency mismatch. Those sometimes lead to serious epitaxial problems and disorders, including cracking, dislocation or bowing. Also, the disorder can occur as epitaxial growth condition is made a bad choice. Rough interface or surface damage is one of the results from bad growth conditions. The largest serious problem is considered as the disorder due to spontaneous generation, for example, inhomogeneity or diffusion between atoms. Those disorders clearly exist in semiconductor, even if high quality semiconductor material is grown essentially.

1.2.3) Classification of Disorder

Fig1.1 shows four different kinds of disorder. The structural or topological disorder is characterized by the absence of long range order and translational periodicity. In the case of magnetic disorder, the spin exhibits different values at each point on a lattice. A similar situation occurs in dipolar solids and liquids where the dipole moments exhibit orientational disorder. Chemical or compositional disorder characterizes a large class of materials such as alloys, mixtures, composites and porous materials. Finally, vibrational disorder refers to the departure of the instantaneously atomic positions from lattice points due to the thermal vibration of the atoms. Furthermore, the values of physical quantities may be statistically distributed over a structure and hence exhibit disorder [3].

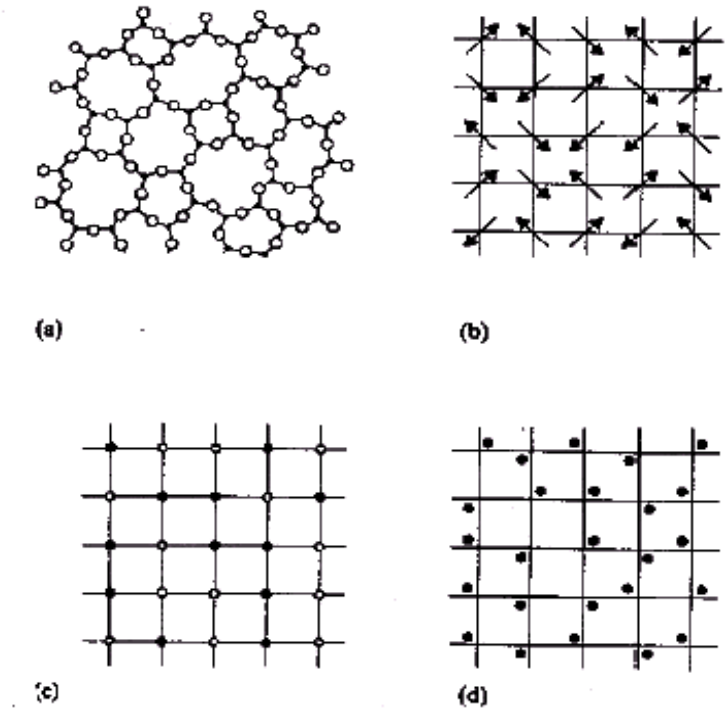

Fig1.1. Several types of disorder (a) structural disorder (b) orientational disorder (spin) (c) compositional disorder (d) vibrational disorder

1.2.4) Macroscopic disorders in semiconductor heterostructures

In semiconductor heterostructures such as quantum wells (QWs) whose width is comparable with the exciton Bohr radius (R_{ex}), low temperature photoluminescence (PL) spectra critically depend on the quality of the structures in terms of the uniformity of composition and the abruptness of interface [4]. Otherwise the linewidths of the spectra are generally used to characterize the interfaces since at low temperatures the principal broadening mechanism is the interface roughness.

In PL measurement, the excitonic recombination is inhomogeneously broadened because of the interface disorder, which includes the island growth and the cation exchange due to atomic interdiffusion. Moreover, because of the alloy disorder, mixed crystals are characterized by exciton linewidth broader than those observed in the pure components. In case of the QWs, if the well widths are larger than R_{ex}, the PL linewidth is determined by the quality of the small-gap material [5]. While for narrow well widths, it is also affected by the quality of the interface and the barrier material.

1.2.5) The disorder effect in semiconductor

Common to all disordered semiconductors is that disorder in the atomic structure leads to specific effects in the electronics structure, such as localization, band tails, defects and polaron formation. The electronic structure determines the electronics properties, for example the carrier mobility, recombination processes,

photoconductivity, contact injection, deep trapping and so on. Understanding the relation between atomic structure, electronic structure and electronic transport is the fundamental goal of research on disordered semiconductors. Also, an interface structure or morphology related to interface disorder between an insulator layer and a semiconductor substrate is important because such structure determine the lifetime of the device.

1.3) The purpose of this work

Recent advance in epitaxial crystal growth techniques such as molecular beam epitaxy (MBE) and metalorganic chemical vapor deposition (MOCVD) have allowed the fabrication of a variety of optoelectronic and microwave devices, many of which have a semiconductor alloy as an important constituent.

However, of this process, disorders clearly but also occur, not only affect in semiconductor device due to incompleteness of growth technique. Structural disorder is an unavoidable feature of any semiconductor crystal. Besides lattice imperfections, residual doping, impurity contamination, which are also present in bulk systems, semiconductor hetero-structures, exhibit potential fluctuations at the interfaces (usually referred as interface roughness) arising from local variations of the layer thickness or alloy composition [6]. Interface roughness plays indeed a very important role in the physics of quantum wells in terms of both applicative and fundamental points. In particular, disorder plays a crucial role in the case of a QW embedded in a resonant optical cavity where the coherent exciton/ polariton are the

basic physical picture of view.

A point of this time, it has become necessary to devise techniques to characterize their quality as determined by the extent of already presented disorder. There exist a number of experimental techniques to estimate disorder in a particular crystal. One of the most useful techniques for obtaining information concerning the quality of the semiconductor is photoluminescence spectroscopy. Generally, the excitonic linewidth in semiconductor alloys are considerably broader than those observed in their components. This broadening has been attributed to compositional disorder in the alloys due to the presence of intrinsic disorder in alloys, transition will be broadened due to concentration fluctuations in the alloy on a local scale which cause the changes in the values of energy of conduction band, E_c (r_0) and energy of valence band , E_v (r_0) [5,7]. High X-ray diffraction is also a very convenient, nondestructive technique for obtaining the information of lattice disorder and structural characterization of the degree of ideality of semiconductor. From the analysis of the rocking curve, information on the period thickness and composition of the layer and information about periodicity and disorder can be obtained. It is reported lattice disorders near crystal surface, resulting from processes such as impurity diffusion, lattice distortion. Those disorders have been studied with X-ray diffraction methods [8].

The present time, although several studies have performed about disorders, those have not clearly distinguished the difference between disorder and defect. Moreover, those have not explained the origins of the disorder yet.

In this thesis, it has been investigated how to estimate several types of disorder using PL, HRXRD and Hall effect measurement. Also, the origins of disorders have been discussed in terms of various physical properties such as optical, electrical, structural properties. The purpose of this thesis is to control and reduce the disorders in semiconductors due to improve the semiconductor device performance up to theoretical limits.

In chapter 2, The principles and used equipments of three methods to evaluate the disorders, photoluminescence, high resolution X-ray diffraction and hall effects measurement was introduced.

In chapter 3 and chapter 4, $Zn_{1-x}Cd_xSe$ and $Zn_{1-x}Cd_xTe$ QW are investigated in terms of PL linewidth broadening, respectively. The results calculated from theoretical models related to composition and interface disorder are compared with experimental values.

In chapter 5, structural qualities of GaN substrate (~1mm) are investigated using HRXRD measurement. Lattice disorder such as mosaicity, tilt, twist and bowing substrate is evaluated by several XRD skills. Also, the surface damage layers originated from polishing defects is not only observed using PL spectra, but also tried to remove using chemical etching.

In the last chapter, GaN thin film grown by HVPE is investigated using T-dependent Hall effect measurement, HRXRD. The results explain relationship between weak disorders such as defect, dislocation and electrical transportation using `potential barrier` model.

Reference

[1] Disordered Alloys : *Diffuse scattering and Monte Carlo Simulations*. pp1

[2] Aharon Kapitulnik, *Physics of Disordered Systems*

[3] Elliott, *S. R, Physics of Amorphous Materials*, Longman, London (1984)

[4] J. Singh, K. K. Bajaj, Appl. Phys. Lett 44, 805 (1984)

[5] J. Singh, K. K. Bajaj, Appl. Phys. Lett. 48, 1077 (1986)

[6] M. Gurioli, F. Bogani, D. S. Wiersma, Phys. Rev. B, vol 64, 165309

[7] A. A. Toropov, J. P. Bergman, J. Crystal. Growth 184/185 (1998) 293

[8] A. Fukubara, Y. Takano, J. Appl. Cryst (1997)10 p287-290

Chapter 2. Experimental

2.1) Epitaxial growth

Epitaxial growth means a technique to deposit the crystal with single orientation on substrate. Consequently, the epitaxially grown layer should exhibit the same crystal structure and the same orientation as the substrate. Fig.2.1 shows surface processes occurring during film growth. The substrate crystal surface is divided into so-called crystal sites where the impinging atoms may interact. Each crystal site is a small part of the crystal surface characterized by its chemical activity. A site may be created by a dangling bond, vacancy, step edge and so on.

Epitaxial growth is generally occurred by three possible modes of crystal growth on surfaces. These modes are illustrated schematically as shown in Fig.2.2. In case of Volmer-Weber mode, small clusters are nucleated. This happens when the physisorbed atoms are more strongly bound to each other than substrate. The layer-by-layer, Frank-van der Merwe mode, displays the opposite characteristics because the atoms are more strongly bound to the substrate than each other. The first atoms complete monolayer on the surface, which becomes covered with less tightly bound second layer. The layer plus island, Stranki-Krastanov, growth mode is an intermediate case. After completing the first monolayer or a few layers, subsequent layer growth is unfavorable and islands are formed on the grown layers. There are many possible reasons for the mode to occur and there exists almost factor which prevents decrease of binding energy for layer-by-layer growth [1].

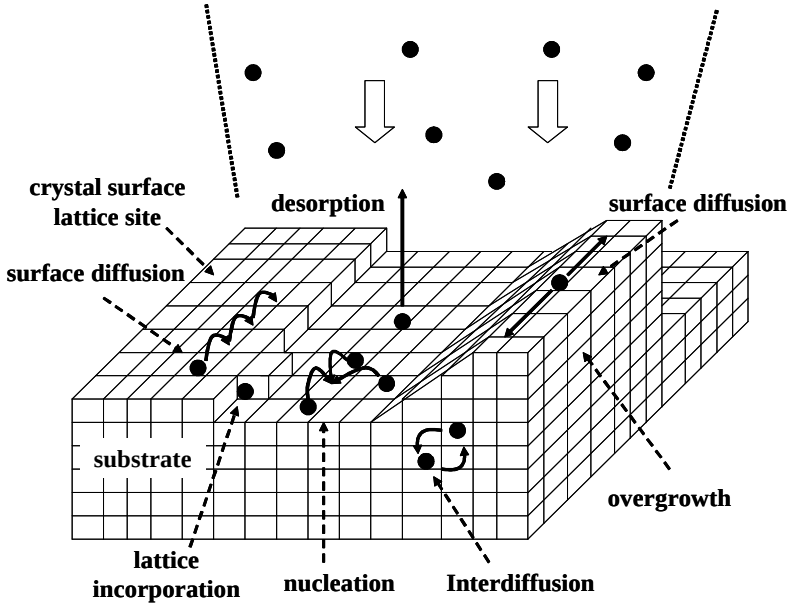

Fig.2.1 Schematic illustrations of the surface process occurring during growth.

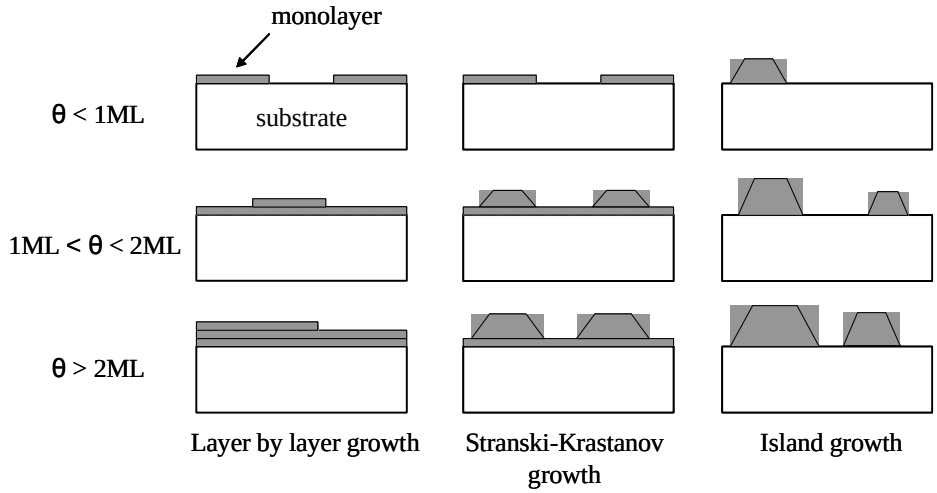

Fig.2.2. Three modes of epitaxial growth θ represents the coverage in monolayers.

2.2) Photoluminescence spectroscopy (PL)

2.2.1) photoluminescence measurement

Photoluminescence is one of the most sensitive nondestructive methods of analyzing both intrinsic and extrinsic semiconductor properties. The method is particularly suitable for the characterization of the centers responsible for shallow donor and acceptor species which control the electrical properties of the layers, as well as near-band-gap luminescence. The PL setup used in this work is shown schematically in Fig. 2.3. Basically, it consists of excitation light sources, a spectrometer, a detector, and a low-temperature cryostat. As an excitation sources, the 325 nm line of He-Cd laser is used for widegap material. When the laser beam was focused on a sample, the laser power density was around 200mW/cm^2. For the low temperature cryostat, He compressor was used, which is necessary to obtain the information by minimizing thermally-activated nonradiative recombination processes and thermal line broadening.

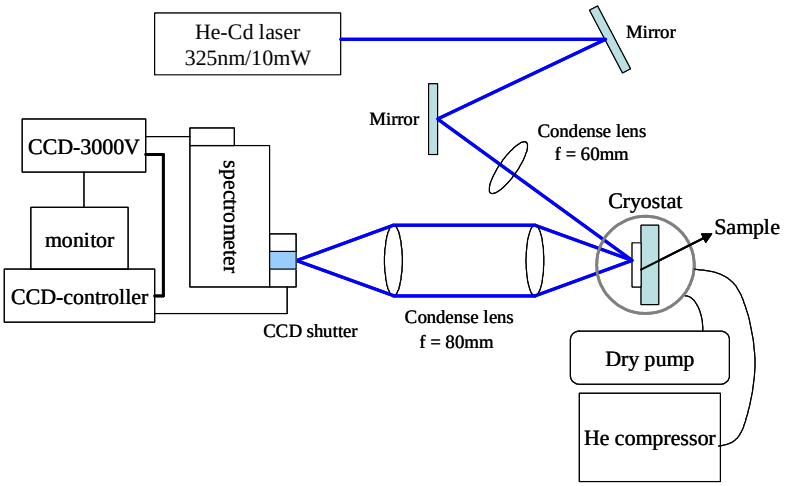

Fig.2.3 Experimental setup used for photoluminescence measurements

2.2.2) Recombination process of Photoluminescence

Radiative recombination takes place when the semiconductor is under a non-equilibrium condition [2]. After excess electron-hole pairs of their equilibrium number are created in the crystal by means of external sources, they relax rapidly to states near the minimum of the conduction band in the case of electrons and near the maximum of the valence band in the case of holes. The carriers may be considered to be in quasi-thermal equilibrium and their distribution can be represented by invoking quasi-Fermi levels. The recombination process can be divided into several processes. CV is transition from the conduction band to the valence band, X is free exciton, D^0X and A^oX are excitons bound to neutral donors or acceptor respectively, CA is transition from conduction band to an acceptor, DA is transition from donor to acceptor, Deep is transition at the deep state in the middle of energy gap. The major features that appear in the photoluminescence spectrum are shown in Fig.2.4 and all these recombination processes are represented schematically in Fig.2.5 [3].

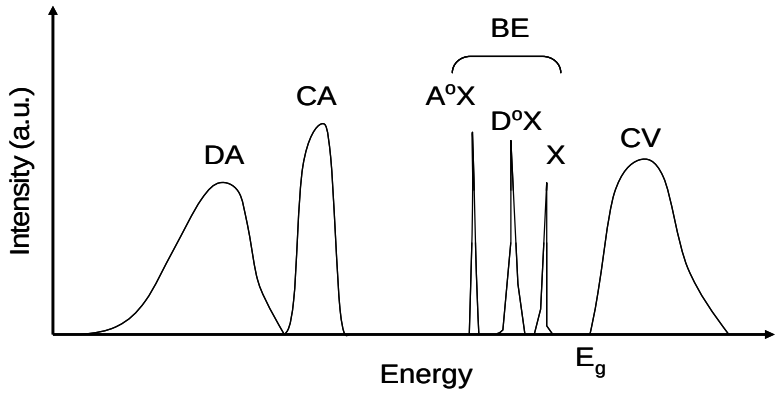

Fig. 2.4 Main features of near band edge photoluminescence spectrum.

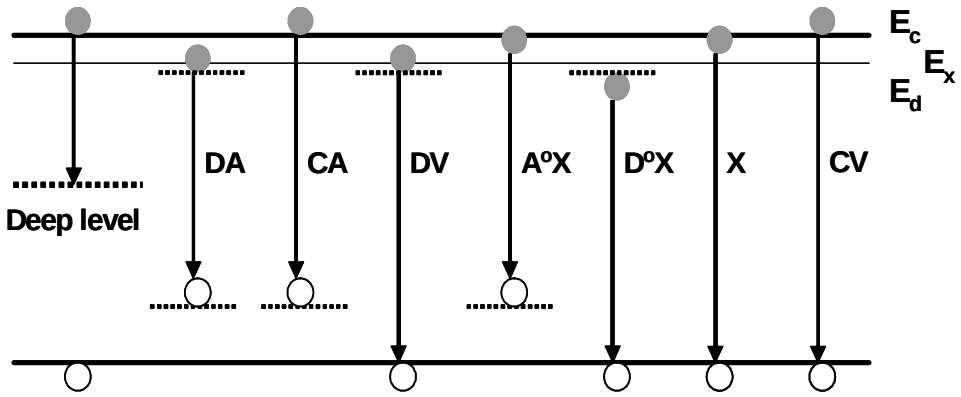

Fig. 2.5 Schematic diagram of recombination processes.

Direct transitions from the conduction band to the valence band are usually observed at temperatures well above 100K. This recombination occurs in the sample with high quality and direct transition. The photon energy $h\nu_{CV}$ in case of band to band recombination is as same as band-gap E_g.

$$h\nu_{CV} = E_g \tag{1}$$

Recombination of electrons and holes through free (X) and bound excitons (BEs) are the processes to appear in the near-gap luminescence spectra as the donor or acceptor concentrations increased. Free exciton occurs due to coulombic interaction between electron and hole. Photon energy $h\nu_x$ of free exciton is such as

$$h\nu_x = E_g - E_x \tag{2}$$

The following E_x is the exciton binding energy

$$Ex = \frac{m^*}{\varepsilon^2}\frac{1}{n^2}13.6eV \qquad \frac{1}{m^*} = \frac{1}{m_e} + \frac{1}{m_h} \tag{3}$$

Satellite spectra `two electron` and `two hole` transitions may be considered when the A^oX and D^oX states are inadequately resolved. In this case the following transitions are observed.

$$D^oX \rightarrow D^o(2p) + h\nu_{em}\,(D^oX) \quad \text{or} \quad A^oX \rightarrow A^o(2p) + h\nu_{em}\,(A^oX), \tag{4}$$

$D^o(2p)$ and $A^o(2p)$ are excited donors and acceptors. $h\nu_{em}$ (D^oX) and $h\nu_{em}$ (A^oX) is the energy of the emitted photons. These lines appear below the principal bound exciton transitions separated by energies which carry almost the entire chemical shift of the impurity ground state. These transitions are the most suitable for providing information on the donor and acceptor centers.

The recombination process from the conduction band to an acceptor state (CA) is a typical example of a so-called free-to-bound transition. photon energy $h\nu_{CA}$ is such like that.

$$h\nu_{CA} = E_g - E_A \tag{5}$$

E_A is the energy state of the acceptor above the valence band edge. The CA band is mainly broadened by the kinetic energy of the electrons before the recombination. CA transitions provide direct spectroscopic information on the acceptor species present in the semiconductor layer.

The DA recombination processes compete strongly with the A^oX and D^oX transitions in case that the concentration of donor and acceptor species is increased. The electrostatic interaction within the ionized donor-acceptor pair after the

transition is responsible for the coulomb term it the expression for the transition energy.

$$h\nu_{DA} = E_g - (E_d + E_a) + \frac{e^2}{\varepsilon \cdot r} \qquad (6)$$

e is the unit charge and *r* is the separation of a donor-acceptor pair. The term in the equation is responsible for the spectral dispersion into a very large number of discrete lines. Each line is associated with a different discrete value or r allowed by a lattice structure. But this discrete line structure is in most cases smeared out if accompanied by lattice relaxation.

2.2.3) Photoluminescence in heterostructure

The basic element of a superlattice is the single quantum well (SQW). Sometimes the term superlattice is used to periodic structure which can be considered as a set of independent quantum wells. In case of this structure, the barrier layers are thick enough to prevent any coupling between the wave functions which is defined the energy state of the carriers (electrons and holes) confined to the individual quantum wells. The simplest quantum well which appears in superlattices is the rectangular or square-shaped, potential well [4]. Photoluminescence of quantum well is very sensitive to interface disorder. Fig.2.6 shows the model introduced by Weisbuch et al [5]. Superlattices grown with growth interruption is shown in Fig. 2.6(a) In this case, there exists effect of the interface disorder on the luminescence linewidth when the lateral size L_s of the

growth islands is smaller than the exciton Bohr diameter. Fig. 2.6(b) shows superlattices grown without growth interruption. When L_s is larger than the exciton Bohr diameter, the exciton experiences only one confinement energy corresponding to L_z–$a/2$, L_z or L_z+$a/2$ and discrete peaks are observed in photoluminescence.

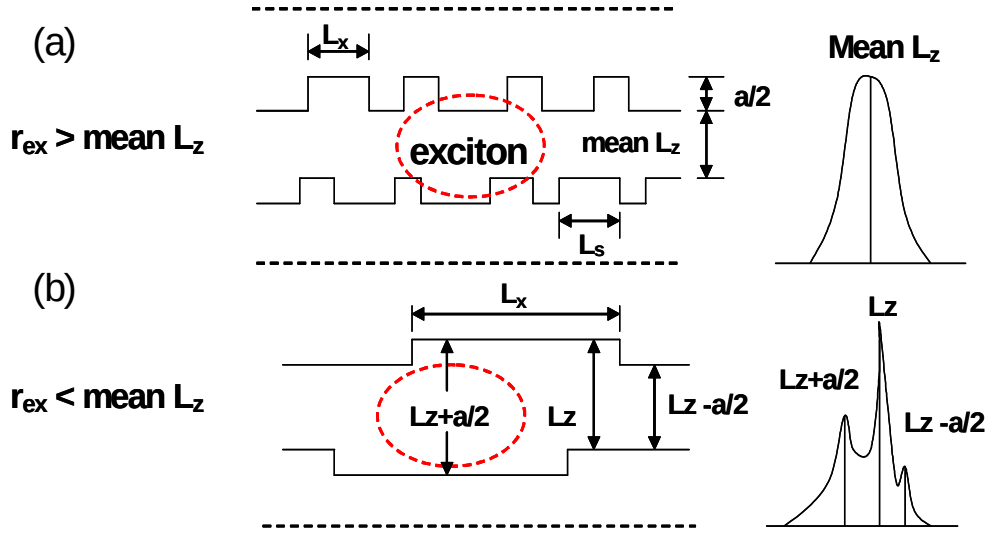

Fig. 2.6 PL spectrum according to relation between exciton and QW`s thickness

The energy levels E_n of carrier with effective mass, m* in infinite potential wells of a width L_z are given by (7)

$$E_x = E_{ni} + \frac{h^2}{8\pi^2 m}(K_x^2 + K_y^2)$$

$$\text{where} \quad E_x = \frac{h^2}{8m_i}\left(\frac{n}{L_z}\right)^2 \qquad n = 1,2,3\ldots \qquad (7)$$

K_x, K_y are here the wave vectors of the particle in the directions parallel to the well walls. The motion of the particle in the z direction is quantized, while in the x

and y directions the particles moves classically. The particle confined to the quantum well exhibit what is known as the quantum size effect, which the E_n is dependent on the width L_z of the well. The photon energy of the n=1 heavy hole exciton recombination is such as

$$h\nu_{CA} = E_{\mathrm{g}} + E_e + E_h - E_b \tag{8}$$

E_{g} is the energy gap, E_e and E_h are the energy shifts of the n=1 electron and heavy hole energy levels and E_b is the binding energy of the exciton. Since this binding energy is typically of the order of 1% of the band gap, its broadening due to a distribution of well width can be neglected.

2.3) Hall effect measurement

2.3.1) Experimental setup of Hall measurement

Electrical characterization can give considerable information about the disorder in terms of purity of epitaxial layers. Such information is important for the evaluation and control of growth parameters used to prepare high quality epitaxial layers for device applications. Electrical characterizations such as mobility, resistivity, carrier concentration are obtained by performing Hall effect measurements.

The Hall measurement setup used in this study is shown in Fig.2.7 schematically. It is consisted of a sample holder including probe stage, a power control unit, a magnetic system, and a low-temperature cryostat. As the probe stage, a home-made tool with four and six probes was used. As the magnetic system is consist of a magnet, a power supply and a Gauss-meter. The temperature control was carried out by the combination low-temperature cryostat and He gas was used to lower temperature until 10K.

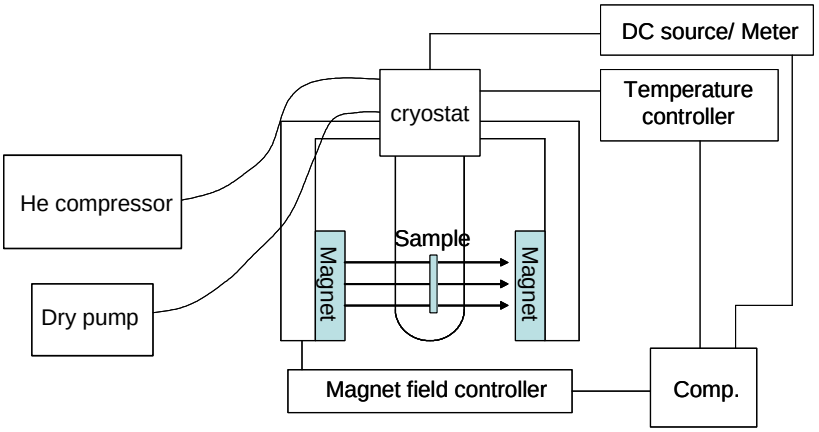

Fig.2.7 Schematic illustration of Hall effects measurement equipment.

2.3.2) Hall effects

The Hall effect is a consequence of the forces that are exerted on moving charges by electric and magnetic fields. The Hall effects is used to distinguish whether a semiconductor is *n* type or *p* type and to measure the majority carrier concentration and mobility [6].

Fig.2.8 shows a sample in the form of a rectangular bar oriented with its longest axis along the x axis. The electric field F is applied along the x axis while the magnetic field B is still along the z axis. According to Lorentz`s law, when electrons start to drift along the x axis under the influence of the electric field, they also experience a force in the y-direction. This results in a current in the y direction although there is no applied electric field in that direction.

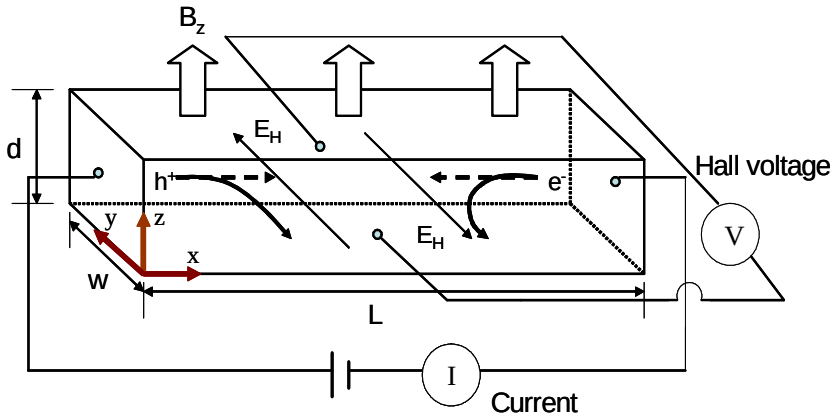

Fig.2.8. The sample geometry for performing Hall measurement.

In a p-type semiconductor, there will be a positive charge on the y=0 surface of the semiconductor. while, in a n-type semiconductor, there will be a negative charge on the y=0 surface. The magnetic field force will be exactly balance by the induced electric field force. This balance may be written as following formula.

$$F = q\,[E + \upsilon \times B] = 0 \qquad (9)$$

The induced electric field in the y-direction is called the Hall field. The Hall field produces a voltage across the semiconductor which is called the Hall voltage. We can write such like that.

$$V_H = +E_H W \qquad (10)$$

E_H is assumed positive in the $+y$ direction and V_H is positive with the polarity shown. In a *p*-type semiconductor, holes are the majority carrier. While, in a *n*-type semiconductor, electrons are the majority carrier. The polarity of the Hall voltage is used to determine whether an extrinsic semiconductor is *n*-type or *p*-type. Then, we can obtain electron, hole concentration in a n-type and p-type semiconductor respectively.

$$n = -\frac{I_x B_z}{edV_H} \qquad p = \frac{I_x B_z}{edV_H} \qquad (11)$$

We can also obtain the low-field electron, hole mobility from (4) respectively.

$$m_n = \frac{I_x L}{enV_x Wd} \qquad m_p = \frac{I_x L}{epV_x Wd} \qquad (12)$$

2.3.3) Van der Pauw method

Samples are often grown in the form of thin epitaxial films on some insulating substrates. The extension of the Hall technique to such thin film was developed by

Van der Pauw [7]. Fig.2.9. shows the Van der Pauw method of measuring the Hall coefficient and resistivity in a thin sample. The current is fed trhough the contacts *3* and *4* while the Hall voltage is measured across the contacts *1* and *2*. The sample shape in Fig.2.9 has the advantage of keeping the current from the Hall voltage contacts.

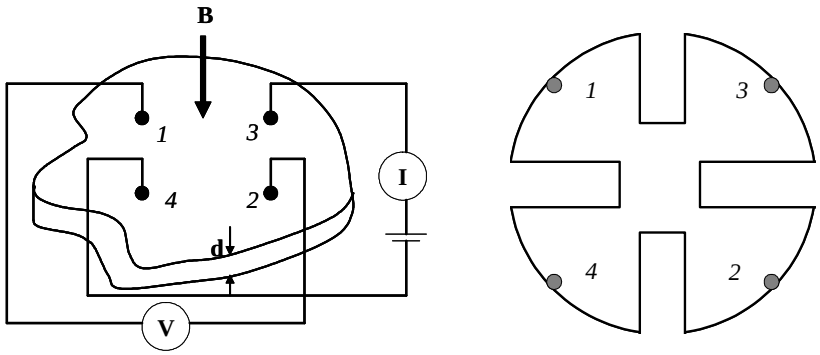

Fig.2.9. Schematic diagrams of Van der Pauw method.

To minimize the error in the measurement of the Hall voltage due to the fact that the current flow may not be perpendicular to the line joining the contacts *1* and *2*, one usually measures the voltage both with the magnetic field $V_{12}(\pm B)$ and without the field $V_{12}(0)$. Van der Pauw shows that Hall coefficient is given by

$$R_h = \frac{[V_{12}(B) - V_{12}(0)]d}{I_{34}B} = \frac{[V_{12}(B) - V_{12}(-B)]d}{2I_{34}B} \qquad (13)$$

d is the thickness of the film, *B* is the magnetic field and I_{34} is the current flowing from contact *3* to contact *4*. The sample resistivity ρ can also be measured with the Van der Pauw method. In this case two adjacent contacts such as 2 and 3

(I_{23}) are used as current contacts while the two remaining contacts are used for measuring voltage (V_{41}). The resultant resistance is defined as $R_{41,23}$.

$$R_{41,23} = | V_{41}| / I_{23} \tag{14}$$

Another measurement is that current is sent through the contacts 1 and 3, then the voltage is measured across the contacts 2 and 4. From the resulting resistance $R_{24,13}$ and $R_{41,23}$, Resistivity ρ can be calculated with following expression.

$$\rho = \frac{\pi d (R_{24,13} + R_{41,23}) f}{2 \ln 2} \tag{15}$$

f is factor that depends on the ratio $R_{24,13}$/ $R_{41,23}$. Usually a large value for this ratio is undesirable and suggests that the contacts are bad or the sample is inhomogeneously doped.

2.4) High-resolution X-ray diffraction (HRXRD)

2.4.1) Experimental setup of HRXRD

High-resolution X-ray diffraction (HRXRD) is a powerful tool for nondestructive ex-situ investigation of epitaxial layers, thickness, the build-in strain and strain relaxation, and the crystalline perfection related to dislocation density.

In study, HRXRD rocking curve were measured by a Philips X`Pert MRD system as shown Fig.2.10. The main components of this instrument are X-ray tube, monochromator, detectors and the sample holder with the crystal. The monochromator consists of blocks made from dislocation-free germanium single crystals. The four crystal Ge (220) monochromator produces a beam with very low divergence and small wavelength spread.

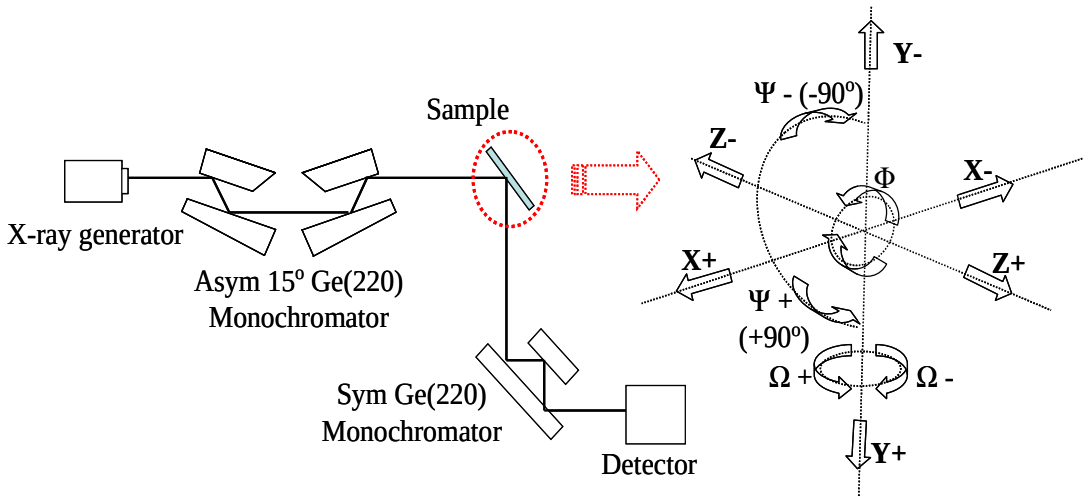

Fig.2.10. Schematic illustration of HRXRD geometry

To investigate structural quality of compound semiconductor, (0002)Ω, (10-11)Ω and (10-11)Φ are usually measured by HRXRD. X-ray power used for

measurement of this study is 40kV, 30mA.

Mosaicity (tilt and twist) was determined by series of X-ray measurement.[8] To determine the tilt angle, rocking curves for (0002), (0004) and (0006) reflection were measured, to determine the twist angle, rocking curves for (0002), (10-13), (10-12), (10-11) and (30-32) reflection were measured [8]. From the tilt, twist angle, it is possible to determine the screw, edge dislocation densities respectively. Detailed procedures calculating dislocation density will be dealt with in the following Chapter 5.

2.4.2) ω scan (rocking curve) and ω-2Θ scan

The simplest and most useful description of crystal diffraction is obtained by Bragg law.

$$2d \sin\Theta = n \lambda \tag{16}$$

Where n is an integer representing the order of diffraction, λ is wavelength, d is the interplanar spacing of the reflecting and Θ is the angle of incidence and of diffraction of the radiation relative to the reflection plane. The requirement for the angle of incidence to equal that of diffraction is directly seen in Fig.2.11.

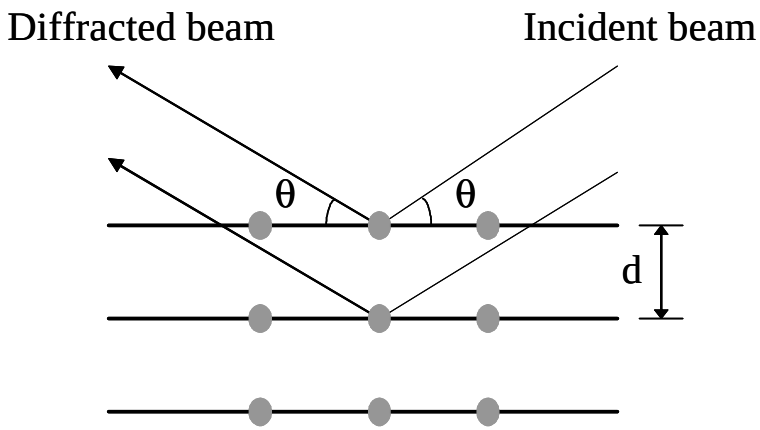

Fig.2.11 Diffraction of a plane corresponding to Bragg law

Diffraction for a given plane and wavelength does not take place over the zero angular range defined by the Bragg law, but over a small finite range. This range, called the `*rocking curve*`, varies tremendously and it shows the structural quality sensitively [9]. Conventional diffractormeters use a ω-2Θ scan for measuring symmetric Bragg reflections. For such a scan, the detector is rotated twice as fast and in the same direction around the diffractometer axis as the sample. In reciprocal space, the motion of sample and detector corresponds to a change of wave vector k_s, which moves along the reciprocal lattice vector G_{hkl}. During the motion, the angle ω between the incident beam and the sample surface changes. In ω scan, the detector is fixed in position with wide open entrance slits and the sample is rotated. In reciprocal space, this corresponds to a path as shown in Fig.2.12 [10].

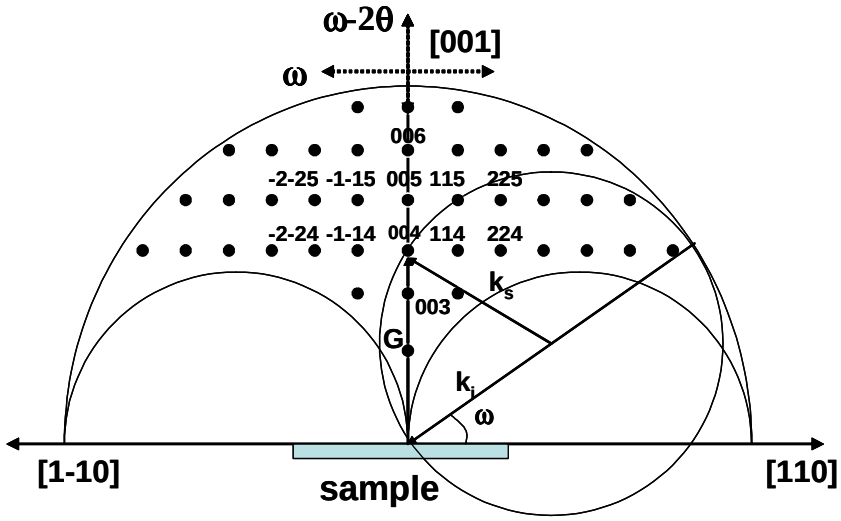

Fig.2.12 Reciprocal space map showing accessible range for Bragg reflection measurements

When we consider about rocking curve of heteroepilayers, there exist differences of diffraction angle between the layer and the substrate, which is caused by tilt ($\delta\theta$) or mismatch (δd). Double or multiple peaks will therefore arise in the rocking curve. Peaks may be broadened by defects if these give additional rotations to the crystal lattice, and there will also be small peaks arising from interference between waves scattered from the interfaces, which will be controlled by the layer thicknesses. The material will show different defects in different regions. Table 1 summarises the influence on the rocking curve of the important parameters [11].

Table1. The effects of substrate and epilayer parameters upon the rocking curve.

Material parameter	Effect on rocking curve	Distinguishing features
Mismatch	Splitting of layer and substrate peak	Invariant with sample rotation
Misorientation	Splitting of layer and substrate peak	Changes sign with sample rotation
Dislocation content	Broadening peak	Broadening invariant with beam size No shift of peak with beam position on sample.
Mosaic spread	Broadening peak	Broadening may increase with beam size, up to mosaic cell size
Curvature	Broadening peak	Broadening increases linearly with beam size Peak shifts systematically with beam position on sample
Relaxation	Changes splitting	Different effect on symmetrical and asymmetrical reflection
Thickness	Affects intensity of Peak	Integrated intensity increases with layer thickness, up to a limit
Inhomogeneity	Effects vary with position on sample	Individual characteristics may be mapped

2.5) Atomic force microscopy (AFM)

The AFM works by scanning a fine ceramic or semiconductor tip over a surface much the same way as a phonograph needle scans a record. The tip is positioned at the end of a cantilever beam shaped much like a diving board. As the tip is repelled by or attracted to the surface, the cantilever beam deflects. The magnitude of the deflection is captured by a laser that reflects at an oblique angle from the very end of the cantilever. A plot of the laser deflection versus tip position on the sample surface provides the resolution of the hills and valleys that constitute the topography of the surface. The AFM can work with the tip touching the sample (contact mode), or the tip can tap across the surface (tapping mode) much like the cane of a blind person. Fig.2.13 shows the schematic illustration of AFM equipment.

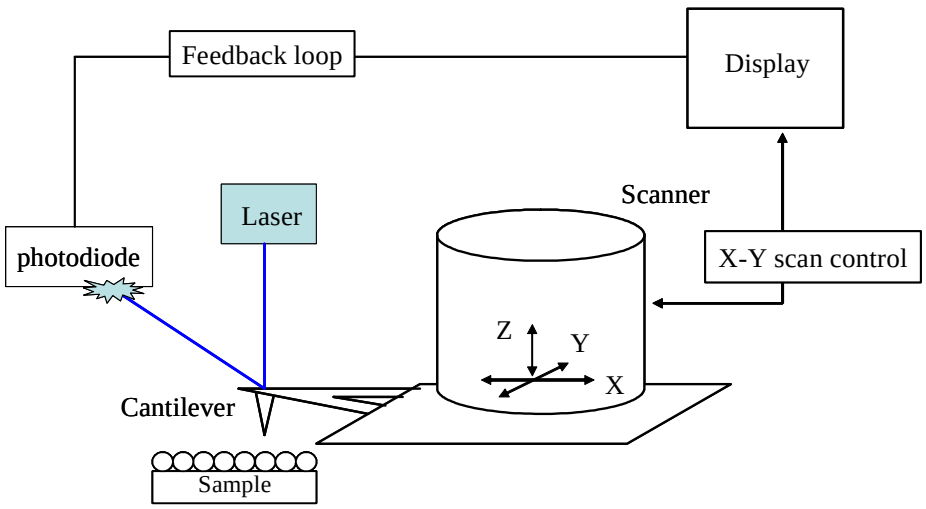

Fig.2.13. Schematic illustration of AFM

Reference

[1] M.A.Herman and H. Sitter, *Molecular Beam Epitaxy, 1st edition* (Springer-Verlag, Berlin, 1998), p9

[2] D. K. Schroder, *Semiconductor Material and Device Characterization* (John Wiley & Sons, Inc., Singapore, 1990), p490

[3] M.A.Herman and H. Sitter, *Molecular Beam Epitaxy, 1st edition* (Springer-Verlag, Berlin, 1998), p184

[4] M.A.Herman and H. Sitter, *Molecular Beam Epitaxy, 1st edition* (Springer-Verlag, Berlin, 1998), p193

[5] C. Weisbuch, R. Dingle. A. C. Gossard, Solid State Commun. 38 (1981) p709

[6] David C. Look, *Electrical characterization of GaAs materials and devices*, John Wiley & Sons, p2

[7] David C. Look, *Electrical characterization of GaAs materials and devices*, John Wiley & Sons, p10

[8] Y. F. Chen, H. J. Ko, S. K. Hong, T. Yao and Y. Segawa, Appl. Phys. Lett 80, 1358 (2002)

[9] D. K. Bowen and B. K. Tanner, *High Resolution X-ray Diffractometry and Topography*, (Taylor & Francis Ltd, London, United Kingdom, 1998), p4.

[10] Gunther Bauer, Wolfgang Richter, *Optical Characterization of Epitaxial Semiconductor Layers*, Springer, p297

[11] D. K. Bowen and B. K. Tanner, *High Resolution X-ray Diffractometry and Topography*, (Taylor & Francis Ltd, London, United Kingdom, 1998), p52.

Chapter 3. Composition disorder of ZnCdSe triple QW

3.1) Introduction

Structural imperfections of quantum well (QW) structures such as interface disorder and alloy disorder affect not only photoluminescence (PL) intensity but also linewidth. It is especially important for alloy quantum wells such as $In_xGa_{1-x}As$ [1], $Cd_xZn_{1-x}Se$ [2] and $In_xGa_{1-x}N$ [3] since these QWs suffer both effects. It should be noted that these QWs provide a lot of merits for the band gap and band offset engineering. However, epitaxy growth of alloy QWs, especially with large x, is still challenging for the crystal growers owing to the increase of lattice constant mismatch and composition disorder. Therefore, efficient method to analyze the structural quality of QWs is required.

There are several ways, which can be applied to this purpose. Transmission electron microscopy (TEM) will give exact information about the structural quality of QWs, but it takes long time and only spatially restricted information is acquired. Meanwhile, Photoluminescence (PL) provides much information about the structural disorder in non-destructive manner. For example, peak intensity is a direct indication of crystal quality, also linewidth broadens when the sample has an imperfection such as compositional disorder and/or structural fluctuation.

In this chapter, structural imperfection of the quantum wells (QWs), $Zn_xCd_{x-1}Se$ is investigated in terms of PL linewidth broadening. Two imperfections of QW structure, alloy and interface disorder are considered. Theoretical calculation

is performed to estimate the linewidth broadening from different origins.

3.2) Theoretical background

3.2.1) Transitional energy of QWs

Fig. 3.1 shows schematic illustration of energy band structure of $Zn_{1-x}Cd_xSe$ QWs.

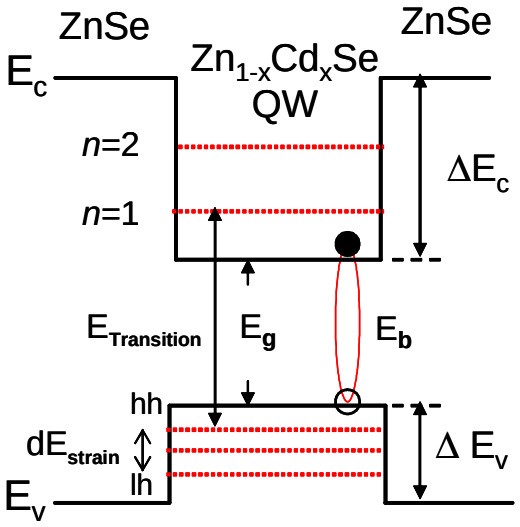

Fig.3.1. Schematic band structure of QW

E_{QW} is the transitional energy of exciton in the QW at low temperature (~10K) by the following formula.

$$E_{QW} = E_g + E_{elec} + E_{hole} - E_b \pm E_s - E_{stokes} \quad (1)$$

Where, E_g is bandgap of unstrained quantum well, E_b is the binding energy due to Columb attraction [1] E_s is energy shift due to lattice misfit. E_{stokes} is energy

shift due to inhomogeneous interface. ΔE_c and ΔE_v is band offset. E_{elec} and E_{hole} is energy due to quantum effect in case of n=1.

3.2.2) Theoretical model related to compositional disorder

It can be shown that compositional fluctuations give rise to fluctuations, ΔE_{ex} of E_{ex}. Fig.3.2 shows the theoretical model related to alloy fluctuation (~compositional disorder) in the QWs.

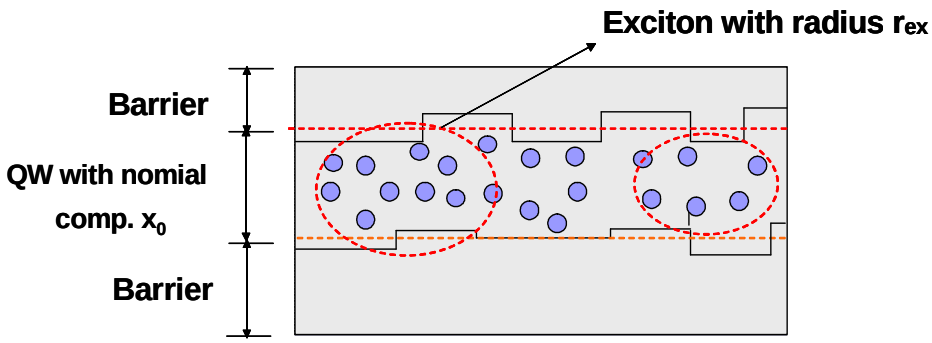

Fig.3.2. theoretical model related to alloy fluctuation

Compositional fluctuation (ΔE_{ex}) can be estimated using the virtual crystal approximation [4,5]

$$\Delta E_{ex}(x, x_0; V_{ex}) \cong (x - x_0)\,\Delta_1 \qquad (2)$$

where, x_0 is nominal composition of the alloy, which is Cd composition in Cd-Zn system, $\Delta_1 = |\partial E_{ex}/\partial x|_{X0}$, and V_{ex} is a critical volume inside which the exciton experiences only a mean crystal potential. The PL full width at half maximum (FWHM) due to alloy fluctuation is given by

$$\gamma_{all} = 2\sqrt{\frac{V_c}{V_{ex}} 1.4 x_0 (1 - x_0)(1 - P_{ex})\Delta_1} \qquad (3)$$

where, V_c is volume per anion site, and V_{ex} is a critical volume of exciton. This formula is considered the dependence on the well width of the exciton localization.[2] If P_{ex} is the probability for the exciton to penetrate into the well barrier, only the fraction (1-P_{ex}) of the exciton is confined in the well.

3.2.3) Theoretical model related to interface disorder

The statistical model also proposed by Singh et al [2,6] is used for the theoretical calculation of PL linewidth broadening. Fig.3.3 shows the theoretical model related to interface disorder in QWs.

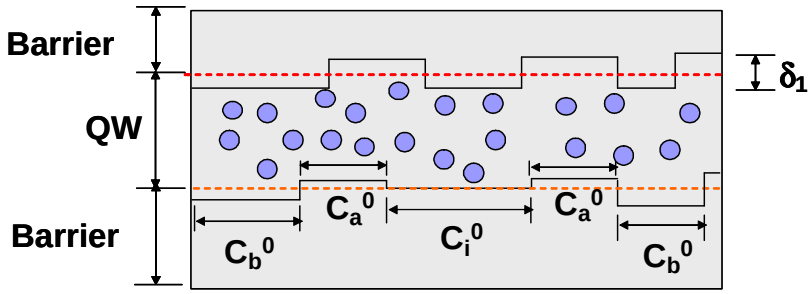

Fig.3.3. theoretical model related to interface fluctuation.

In this model, if z = 0 identifies the position of the ideal interface between the A(z <0) and B(z >0), in the real interface there are islands of the compound B for z <0 and islands of the compound A for z >0. Therefore, real interfaces involve fluctuations δ1 of the QW thickness. The mean concentrations of the islands of

QW and barrier, and of the flat regions of ideal interface are C_{QW}^{0}, $C_{barrier}^{0}$, and C_{i}^{0}, respectively, their lateral extensions are δ_{2QW}, $\delta_{2barrier}$, and δ_{2i}, which is defined as the height of the 2D island. The lateral extent of the exciton wave function is $\rho_{ex.}$ E_{ex} (L) is the exciton recombination energy. $E_{ex}(L)$ diverges for L → 0 in the ideal case of a well of infinite depth, it reaches a finite maximum at L = 0 in the case of a well of finite depth, because of the penetration of the exciton wave function into the barrier material. For the simplification of calculation, it is regarded that $\delta_{2QW} \approx \delta_{2barrier} = \delta_2$ and $\delta_2 < \rho_{ex}$. It has been shown that the exciton line shape in the PL spectra is given by a Gaussian function with full width at half maximum [4].

$$\gamma_{\text{int}} = \sqrt{2}\frac{\delta_2}{\rho_{ex}}\left(1.4\sqrt{C_a^0 C_b^0}\right)\left(C_a^0\Delta^+ + C_b^0\Delta^-\right) \qquad (4)$$

where

$$\Delta^+ = \left.\frac{\partial E_{ex}}{\partial L}\right|_{L_0+\delta L}\cdot\delta_1 \qquad \Delta^- = \left.\frac{\partial E_{ex}}{\partial L}\right|_{L_0-\delta L}\cdot\delta_1$$

L_0 is the mean thickness of the quantum well. $\triangle^+$ and $\triangle^-$ depends strongly on L, $\rho_{ex\ s}$depends more smoothly on L.

3.2.4) General trends of disorder

Fig.3.4(a), (b) shows the general trends of PL linewidth owing to compositional and interface disorder when the Cd–composition is 15, 30, 45% in $Zn_{1-x}Cd_xSe$ QWs, respectively. It is considered δ_1 as 0.5 for this calculation in

case of interface disorder.

γ_{all}, PL linewidth broadening due to alloy disorder, shows that the more increase the well width for a given x_0, the more decrease the probability of the penetration of exciton wave function into the barrier. Therefore, it increases the contribution of the alloy disorder to the PL linewidth. For quantum wells of infinite depth, γ_{int}, PL linewidth broadening due to interface disorder, increases monotonically for decreasing L and becomes infinite for L=0, while for quantum wells of finite depth the value of γ_{int} reaches a maximum and then decreases as L approaches zero (γ_{int} = 0 for L = 0), because penetration of the exciton wave function into the barrier increase.

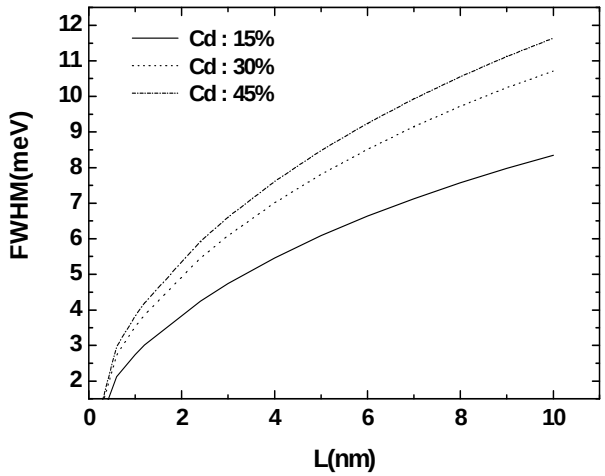

Fig.3.4(a) Composition fluctuation of ZnCdSe QW with various Cd-content

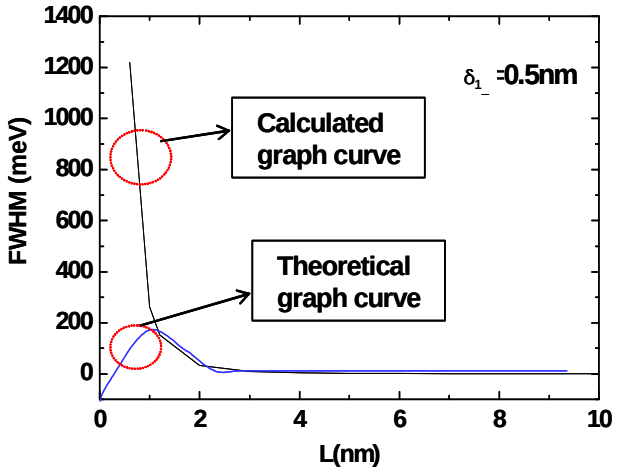

Fig.3.4(b) interface fluctuation of ZnCdSe QW with increase of QW thickness

3.3) Experimental

Fig.3 shows the schematic drawing of ZnCdSe/ZnSe triple QW structure. ZnCdSe/ZnSe QWs were grown on GaAs (001) substrates by molecular beam epitaxy (MBE). GaAs substrate is thermally deoxidized at 580℃ during 10 minutes. Zn-exposure was performed before strating growth. Firstly, ZnSe layer was grown on GaAs substrate. After then, $Zn_xCd_{x-1}Se$ QWs with different thickness and Cd-composition were grown at 280℃. After the growth of triple QW structure, 40 nm thick ZnSe capping layer was grown.

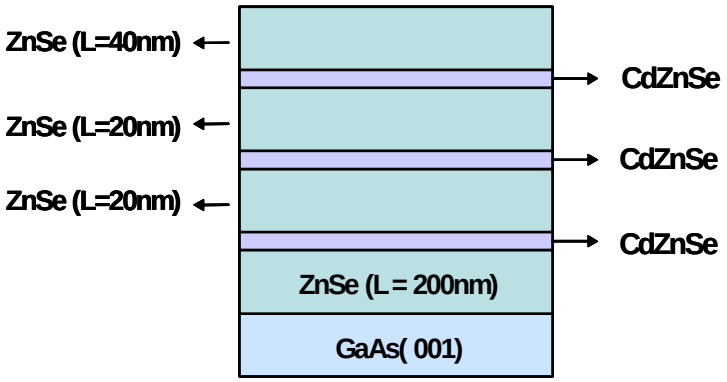

Fig3.. The schematic drawing of ZnCdSe/ZnSe triple QW structure

3.4) Evaluation of compositional and interface disorder (fluctuation)

Fig 3.5 shows transitional energy of QWs with different thickness.

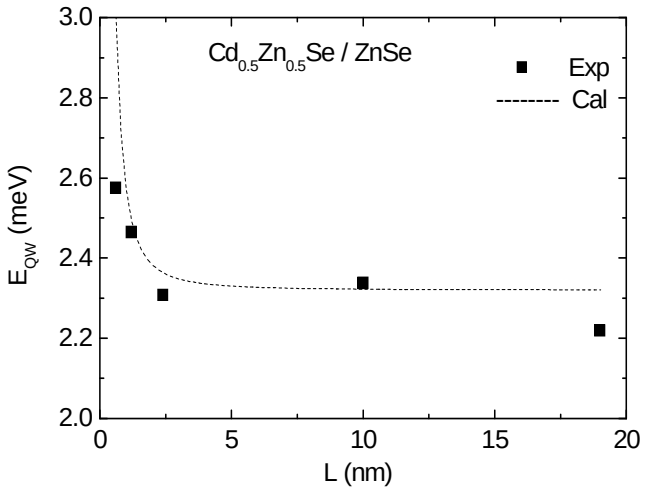

Fig.3.5. Transition energy of $Zn_{0.5}Cd_{0.5}Se$ QW with various thickness

To obtain the E_{QW} with variation of QW width, E_g is calculated using a formula related to $Cd_xZn_{1-x}Se$ [7].

$$E_{g\ CdZnSe} = E_{g\ CdSe} + (E_{g\ ZnSe} - E_{g\ CdSe} - b)(1-x) + b(1-x)^2 \qquad b = 0.301 \qquad (5)$$

In here, *b* is regarded as 0.301, which is the bowing parameter in $Zn_{1-x}Cd_xSe$ QWs. The calculated result shows considerable agreement with theoretical value when the thickness of QW is thinner than 10nm. This indicates high structural quality of the QW sample. The possible reason for difference between two values above 10nm thickness is the Cd/Zn interdiffusion, which is expected to be enhanced at high Cd-composition.

Fig.3.6 shows the PL linewidth of $Zn_{1-x}Cd_xSe$/ZnSe QWs with different Cd-composition. The peak position decreases and PL linewidth increase along with Cd-composition increase. The thickness of QWs is 3.5 nm and surface roughness of samples are 0.81 nm (Cd = 15%), 0.93 nm (Cd = 30%), 0.91 nm (Cd = 45%) respectively. Therefore, the PL linewidth broadening increases due to the increase of alloy disorder. The theoretical linewidth of these samples is listed in Table 1. In the case of QW with 15% Cd-composition, alloy and interface disorder are estimated as 5.34meV and 0.61meV respectively, and total linewidth is calculated as 5.37meV. However, the disagreement increases as Cd-composition increase. The critical thickness of CdZnSe layer will be decreased as Cd-composition increase due to lattice mismatch increase. But it is still much thicker than 3.5nm [7]. Therefore, additional interface fluctuation related to lattice mismatch is hard to consider as shown from surface roughness. We suggest that there exist another reason for PL linewidth broadening, which is not related with interface disorder.

One possible reason is Cd-Zn interdiffusion. Kyutt et al reported that at the interface of CdSe/ZnSe superlattice graded composition CdZnSe alloyeds layer is formed due to Cd-Zn interdiffusion.[8] When one has graded composition CdZnSe layer at the interface, PL linewidth will be broaden due to piled up of transition states from CdZnSe interfacial layer. It is reported that Cd-Zn interdiffusion is occurred up to 4.5 monolayers from the ideal interface at the growth temperature of 290℃ [8], which will increase alloy broadening effect. In our experiment, the difference between theoretical and experimental linewidth values increases as Cd composition increase. Since the possibility of Cd-Zn interdiffusion will increase along with Cd content, the observed linewidth increase can be regarded as the result of interdiffusion.

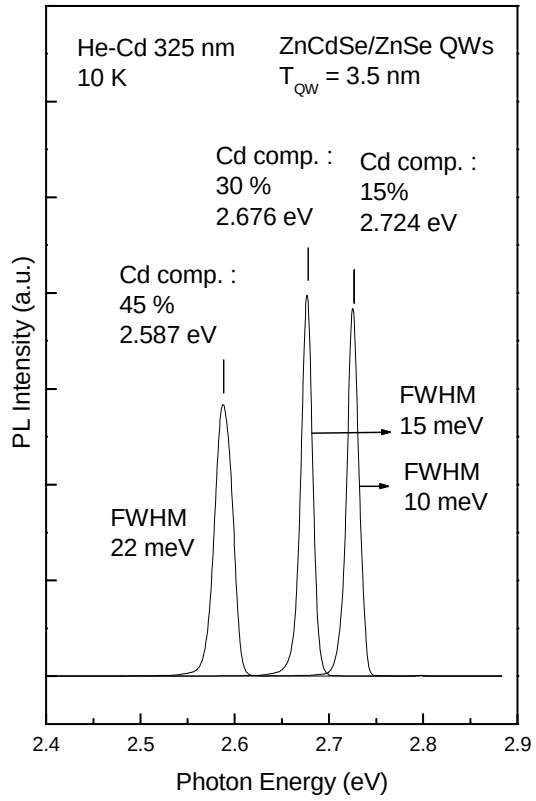

Fig.3.6. PL spectra of $Zn_{1-x}Cd_xSe$ TQW with different Cd composition

Table.3.1. Measured and calculated linewidth of CdZnSe QWs with different Cd composition

Cd Comp.	PL FWHM (meV)	Cal. Alloy disorder (meV)	Cal. Interface disorder (meV)	Total calculated linewidth (meV)
15	9.8	5.34	0.61	5.37
30	14.9	6.85	1.22	6.95
45	22.0	7.12	1.84	7.35

Fig.3.7 shows PL spectra of $Cd_{0.5}Zn_{0.5}Se$ QWs with different QW thickness. It is characterized that broad PL linewidth and linear decrease of luminescence intensity as QW thickness increase. Since both alloy and interface fluctuation is a function of QW thickness, PL linewidth should be changed closely related with QW thickness, however, only a weak relation between QW thickness and linewidth is observed. From the calculation, the total linewidth of a sample with 0.6nm thick QW is estimated as 6.4meV. Large difference between theoretical and experimental values exists similarly to the sample with 45% Cd composition as Table 3.2. Now, it is cleared that a QW with large Cd composition always shows much broader linewidth than theoretical estimation. It strongly indicates additional broadening effect.

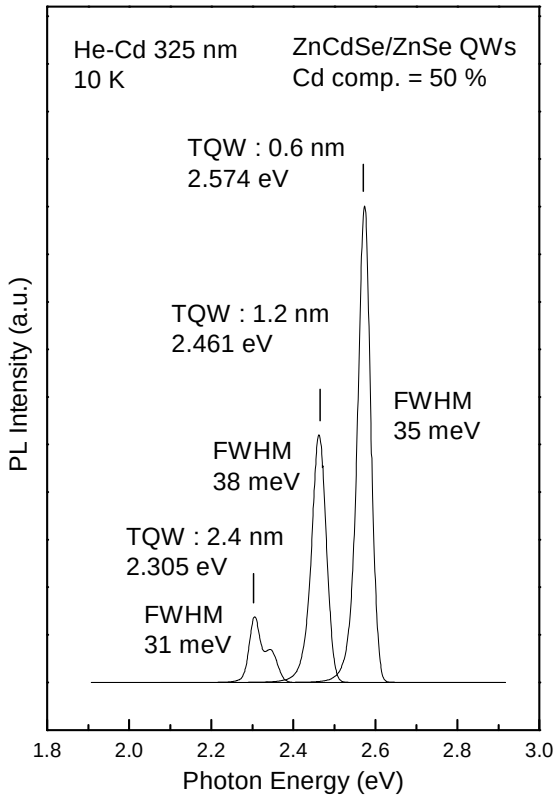

Fig.3.7. PL spectra of $Zn_{1-x}Cd_xSe$ TQWs with different thickness

Table.3.2. Measured and calculated linewidth of CdZnSe QWs with different thickness

TQW (nm)	PL FWHM (meV)	Cal. Alloy disorder (meV)	Cal. Interface disorder (meV)	Total calculated linewidth (meV)
2.4	31	5.95	19.06	19.96

There are two possible reasons for the extra-broadening of PL linewidth. In the bulk single crystal of the alloy CdZnSe have the zincblende structure for $x<0.3$, the hexagonal wurtzite structure for $x>0.5$, and mixed phases for $0.3<x<0.5$ [9]. When the mixed phase growth is occurred during the growth not only drastic decrease of luminescence intensity but also obvious change of RHEED pattern will be observed. However, in our experiment, the PL intensity of QWs only smoothly decreased, also any proof of structural change was not observed from RHEED observation during the growth. Moreover, there is a report about the epitaxial growth of zincblende CdSe by MBE[10], which indicates zincblende CdZnSe can be grown under adequate growth conditions.

3.5) Conclusions

We have studied the PL linewidh broadening of CdZnSe QWs. Measured and calculated PL linewidth show agreement whe the Cd-composition is low. However, disagreement increases Cd-composition increase. As a possible reason for the calculated additional linewidth broadening, Zn/Cd interdiffusion is suggested, which will be enhanced at high Cd contents QWs. Therefore, to reduce the extra-broadening of PL linewidth, one should consider the way not only to improve structural quality but also to minimize interdiffusion of atoms.

Reference

[1] A. Patane, A. Polimeni, M. Capizzi, and F. Martelli, Phys. Rev. B 52(4) 2784(1995)

[2] U. Neukirch, D. Wecknedrup, J. Gutowski, D. Hommel, G. Landwehr, J. Cryst. Growth 138 861 (1994)

[3] Y. Narukawa, Y. Kawakami, S. Fujita, S. Nakamura, Phys. Rev. B 55 (4) R1938 (1997)

[4] O. Goede, L. John, and D. Henning, Phys. Status Solidi B89 K183 (1978)

[5] J. Singh and K. K. Bajaj, J. Appl. Phys. 57, 5433 (1985)

[6] J. Singh, K. K. Bajaj, and S. Chauduri, Appl. Phys. Lett. 44 805 (1984)

[7] J. Wang, X. Wang, Z. Q. Zhu, and T. Yao, J. Phys. Conens. Matter 7, 5835 (1995)

[8] R. N. Kyutt, A. A. Toropov, T. V. Shubina, S. V. Sorokin, S. V. Ivanov, M. Karlsteen, M. Willander, Appl. Surf. Sci. 166 (2000) 341

[9] A. S. Nasibov, Yu. V. Korostein, P. V. Shapin, L. G. Suslina, D. L. Fedorov, and L. S. Markov. Solid State Communication 71, 867 (1989)

[10] N. Samarth, H. Luo, J. Furdyna, S. B. Qadri, Y. R. Lee, A. K. Ramdas, and N. Otsuka, Appl. Phys. Lett. 54(26), 2680, (1989)

Chapter 4. Interface and composition disorder of high quality ZnCdTe multiple quantum wells

4.1) Introduction

Photoluminescence (PL) spectroscopy is one of the most useful technique to obtain information on the quality of semiconductor alloys, quantum structures and nanostructure as stated in chapter 3. Physical quantities obtained from PL such as peak intensity, line width, line shape, and temperature/temporal variation of these quantities give valuable information about the sample. For example, peak intensity is a direct indication of crystal quality, also line width broadens when the sample has an imperfection such as compositional disorder and/or structural fluctuation. Since these imperfections have large influence on the performance of semiconductor device, there were many studies to estimate the effect caused by imperfection.

In this study, PL line width broadening due to composition/ interface disorder of ZnCdTe/ZnTe MQW is studied. RHEED intensity oscillations are used to prepare high quality material, which is inevitably needed for this study. Also, theoretical calculation [1, 2] is performed for the quantitative estimation of the imperfection.

4.2) Experimental

ZnCdTe/ZnTe multiple quantum wells (MQW) was grown on ZnTe (001) substrate by using MBE. ZnTe substrates were chemically etched by Br (3vol.%): Methanol solution and deoxidized by diluted HF just before to be introduced into the load lock chamber [3]. Thermal treatment was performed at 350℃ during the growth thermal treatment (2×1) reconstruction pattern was observed in [110] direction. The reflection high energy electron diffraction (RHEED) pattern was almost streaky at the end of thermal treatment and it becomes completely streaky when the growth starts. The buffer layer of 50nm was grown at low temperature of 240℃, then the substrate temperature increased to 300℃ for the low temperature buffer growth. RHEED intensity oscillations were used for the control of both QW layer thickness and Cd composition. High resolution X-ray diffraction (HRXRD) measurement was used to confirm to structural quality and photoluminescence (PL) spectroscopy was used to investigate the effect of composition and interface fluctuation on the luminescence linewidth.

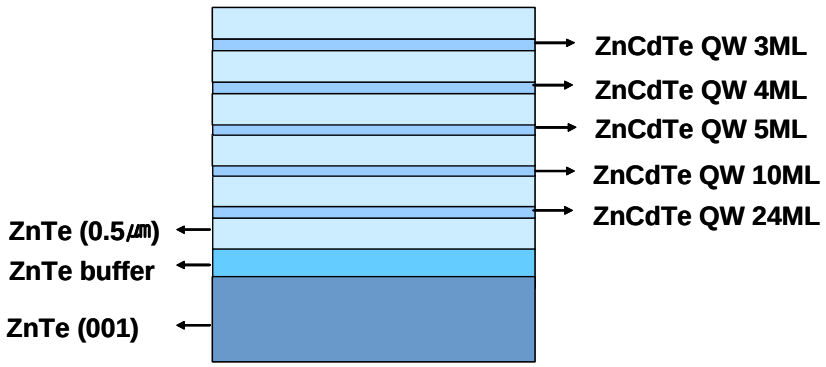

Fig.4.. The schematic drawing of ZnCdTe/ZnTe multiple QWs

4.3) The Control of QW thickness and composition

Using the RHEED intensity oscillation, it is possible to precisely control thickness and Cd-composition of QWs. Fig 4.1 shows RHEED intensity oscillation frequencies when $Zn_{1-x}Cd_xTe$ QW is grown. Cd composition is obtained from the following formula [4].

$$x = \frac{f_{Zn_{1-x}Cd_xTe} - f_{ZnTe}}{f_{Zn_{1-x}Cd_xTe}} \quad (1)$$

where, f is RHEED intensity oscillation frequency, which is corresponding to the 1/(oscillation period) The Cd composition is estimated as 21% in average and the composition variation between QWs is less than 0.7%. In this study, 1ML is corresponding to 3.09Å.

After the growth of ZnCdTe QW layer, Cd shutter is closed at the peak RHEED intensity point, however, the RHEED intensity oscillation continues and the intensity is almost recovered to initial value.

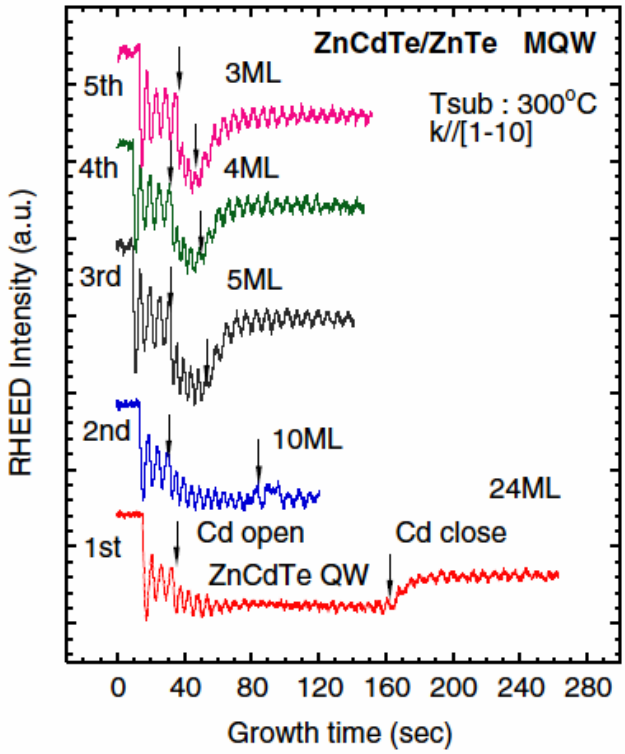

Fig. 4.1 RHEED intensity oscillation of ZnCdTe QWs

When we start the growth of ZnCdTe, RHEED intensity oscillation amplitude damped as the growth proceeds. It could be interpreted in terms of the Ⅵ/Ⅱ ratio change due to the addition of Cd adaptoms on the surface [5]. Since Ⅵ/Ⅱ ratio is changed by the addition of Cd, which brings RHEED intensity change [6]. Also, the reflection intensity of specular spot from ZnTe and CdTe surface will be different. Therefore, specular spot intensity, during the intensity oscillation transition, will occur. However, it should be noted those explanations do not indicate growth mode change or surface degradation because when we close Cd

shutter RHEED intensity oscillation continued and the intensity recovered to the initial value.

4.4) Structural characterization of ZnCdTe MQW

Fig.4.2 shows HRXRD result of ZnCdTe/ZnTe QWs. Satellite peaks by multiple diffractions are observed, which indicates that the QWs have abrupt interface with high crystallinity. The dotted curve in Fig.4.2 is a simulated one. Considerable agreement is observed between measured and simulated curve. The small mismatch in the position of highest satellite peak, especially in the low angle side, may be originated from the fact that simulation just considers completely strained structure.

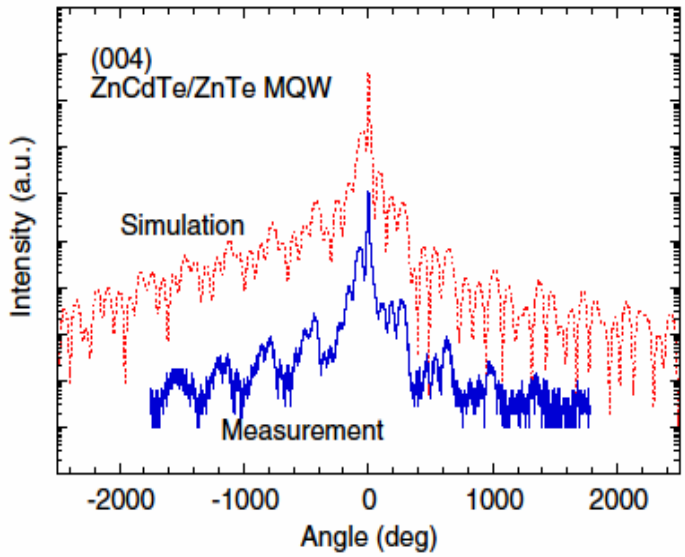

Fig.4.2. HRXRD rocking curve of ZnCdTe/ZnTe 5QW structure

4.5) The alloy/interface disorders in ZnCdTe MQW

Fig.4.3 shows the photoluminescence (PL) spectrum of ZnCdTe/ZnTe multiple QW at 10 K. Two peaks at 2.341 eV, 2.352 eV are assigned to bound excitons from ZnTe. Also five peaks from 2.332 eV to 2.252 eV are ascribed to MQW. In a disordered structure, the line shape of low-temperature PL spectra depends on the uniformity of composition and abruptness of the interfaces. The statistical models related to alloy/interface disorder have been already suggested in chapter 3. In fact, the exciton recombination is inhomogeniously broadened due to the interface disorder caused by interface roughness. The linewidth is calculated as a function of the island size and density (surface coverage of islands) in terms of interfacial disorder. When we regard the 2D island height as 1ML, the PL linewidth (34 meV) of 5 ML thick QW is well corresponds to theoretical value (33 meV) from interface disorder and 2.2 meV from alloy disorder). As previously mentioned, RHEED intensity oscillations were used to grow MQW structure and HRXRD measurement shows high interfacial quality. Since 1ML can be regarded as very close value to minimum step height, it may be adequate approximation. While the QWs thicker than 5 ML have much broader line width to be explained by interfacial fluctuation, which indicats alloy fluctuation should be considered to explain the linewidth. Also, the QWs of thinner than 5 ML have narrower line width than the theoretical value. It should be interpreted with the consideration of the relationship between QWs thickness and exciton radius. Patene et al. reported that when the thickness of QW layer becomes small in compare to the Bohr radius

of exciton, PL linewidth broadening due to interface fluctuation will be considerably decrease [7]. The Bohr radius of 3-dimensional exciton in ZnTe is reported as large as 11.5 Å [8]. It implies that the Bohr radius of 2-dimensional exciton in ZnCdTe QW may be larger than this value. Actually, it was reported that the Bohr radius of exciton in ZnCdTe is as large as 5 nm [9,10]. The compositional inhomogeneity will have dominant effect especially when ZnCdTe QW has large Cd content. However, if one compared the QWs with same Cd content, thicker one will have broad full width at half maximum (FWHM), since total amount of compositional disorder in an exciton will increase. In the model related to compositional disorder, the P_{ex} is the probability for the exciton wavefunction to penetrate into the barrier. Therefore, only the $(1-P_{ex})$ of the exciton is confined in the quantum well. Theoretical values for the alloy fluctuation monotonically increase. In the case of 24 ML thick QW, the calculated value (4.7 meV) is very close to the experimental value (6.5 meV). It strongly indicates the interface disorder is almostly diminished, also the FWHM of 24 ML thick QW is mostly originated from alloy disorder.

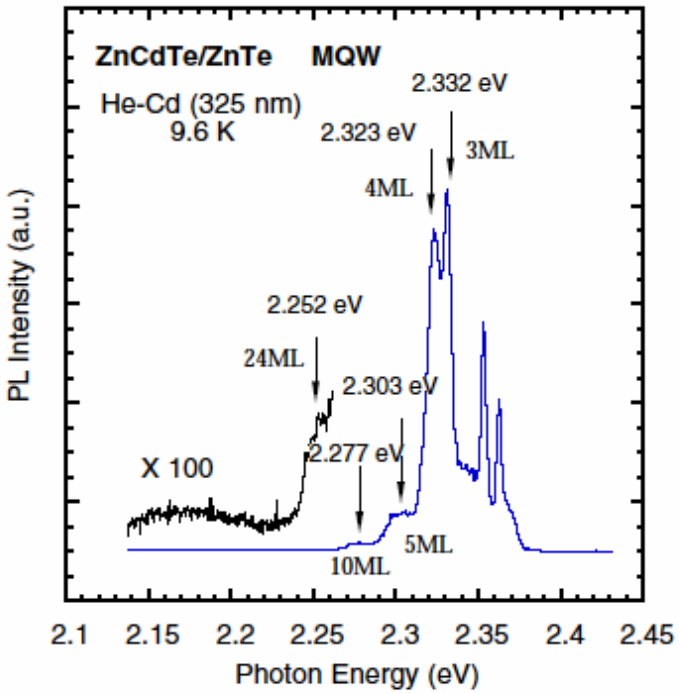

Fig.4.3. Low temperature PL spectra of ZnCdTe/ZnTe 5QW structure

Table.4.1. Theoretical and experimental linewidth of ZnCdTe/ZnTe 5QW

QW	QW Thickness (nm)	Experimental Result (meV)	Theoretical results	
			Alloy disorder (meV)	Interface disorder (meV)
3ML	0.92	5.0	1.7	155
4ML	1.24	7.3	1.9	65
5ML	1.54	33.8	2.2	33
10ML	3.10	16.5	3.1	4.2
24ML	7.42	6.5	4.7	0.3

4.6) Conclusion

Photoluminescence linewidth broadening of ZnCdTe/ZnTe multiple quantum wells has been investigated. RHEED intensity oscillations are used to grow highly defined sample. Oscillation damping, presumably due to Ⅵ/Ⅱ ratio change and enhanced migration of Cd adaptoms, is observed during the growth of ZnCdTe QW layers. Theoretical calculation is performed under the assumption of minimum interface disorder (1ML). The results show that when QW thickness is considerably smaller than Bohr radius of exciton, PL line width have much smaller value in compare to experimental result. However, if the QW thickness is similar or larger than exciton radius, the experimental results show considerable agreement with the calculated values.

Reference

[1] J. Singh and K. K. Bajaj, Appl. Phys. Lett 44 (11), 1075 (1984)

[2] D. J. Olego, J. P. Faurie, S. Sivananthan, and P. M. Raccah, Appl, Phys. Lett.47(11), 1172 (1985)

[3] J. H. Chang, M. W. Cho, H. M. Wang, H. Wenisch, T. Hanada. T. Yao, K. Sato, O. Oda, Appl. Phys. Lett. 77(9) 1256 (2000)

[4] M. A. Herman and H. Sitter, *Molecular Beam Epitaxy*, Springer-Verlag, p291

[5] M. A. Herman and H. Sitter, *Molecular Beam Epitaxy*, Springer-Verlag, p145

[6] T. Yao, Z. Zhu, K. Uesugi, S. Kamiyama, and M. Fujimoto, J. Vac. Sci. Technol. A8, 997 (1990)

[7] A. Patane, A. polimeni, M. Capizzi, F. Martelli, Phys. Rev. B 52(4) 2784 (1995)

[8] P. Y. Yu, M. Cardona, *Fundamentals of semiconductor*, Springer, p272

[9] V. I. Kozlowsky, Yu. G. Sadofyev, and V. G. Litvinov, 8th Int. Symp. “Nanostructures:physics and technology”, St Petersburg, Russia, p10 (2000)

[10] H. J. Lozykowski and V. K. Shastri, J. Appl. Phys 69, 3235 (1991)

Chapter 5. Defect formation due to structural disorder of GaN substrate

5.1) Introduction

Epitaxial films having a large lattice mismatch with their substrate will have mosaic structure of slightly misoriented sub-grains. Although epitaxy is generally performed with mismatchies, thus the epi-layers usually exhibit a mosaic structure. Moreover, the large difference of thermal expansion coefficients between epilayers and foreign substrates induce serious wafer bowing and cracking [1,2]. Actually, the specific features originated from lattice disorders such as mosaicity, tilt, twist and bowing give serious influence on device performance and production yield. The quantity of such a disorder is usually expressed by the full width at half maximum (FWHM) of X-ray rocking curves. However, in the majority of practical cases, the substrate is usually substantially thicker than the absorption length of the X-ray thereby precluding this direct measurement. Yun et al. have reported that X-ray rocking curves of distorted free-standing GaN substrates are seriously broadened [3].

In this chapter, we have investigated the substrate with structural disorder from X-ray rocking curve (XRC), also, will explain how to evaluate the lattice disorder such as tilt, twist and bowing for GaN substrate.

5.2) Theoretical background

5.2.1) Mosaicity in Hexagonal structure

Mosaic crystals can be characterized by means of tilt and twist angle and average size of the mosaic block. The tilt describes the out of plane rotation of the blocks and the twist describes the in-plane rotation. Fig.5.1 shows schematic illustration of tilt and twist in hexagonal structure.

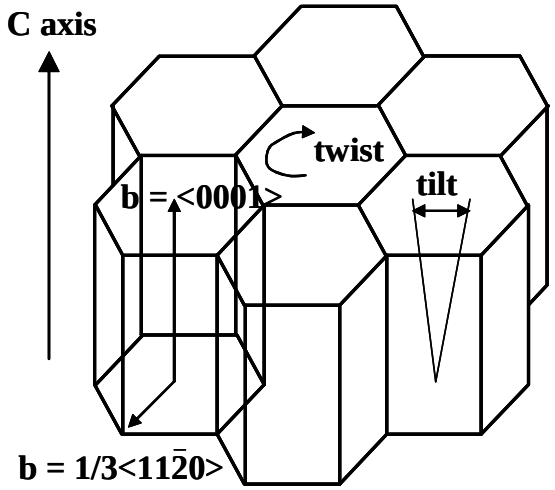

Fig.5.1. Schematic illustration for mosaic structure in terms of tilt, twist angle

5.2.2) Evaluation of tilting

Tilt angle can be determined by so-called Williamson-Hall plot (W-H plot). The concept is based on the fact that the broadening of the rocking curves of the symmetric reflection (0002), (0004) and (0006) in a wurtzite structure is influenced only by tilt and small correlation length parallel to the substrate surface. Bending or heterogeneous strain does not influence the peak broadening owing to the small

acceptance angle of the detector in modern HRXRD apparatus. As the broadening in reciprocal space due to tilted crystal is proportional to the scattering order and the broadening due to a small correlation length is independent of the scattering vector, a graphical separation of these two effects is possible by recording higher order reflections. If a linear superposition of both effects is assumed, a separation analogous to the W-H plot can be performed, where $\beta_\Omega \sin(\theta)/\lambda$ is plotted against $\sin(\theta)/\lambda$ for each reflection and fitted by a straight line [4]. Here, β_Ω is the integral FWHM of the measured profile, λ is X-ray wavelength (=1.540562Å), and 2Θ is the scattering angle. The slope of the (fitted) line is a direct value of the tilt angle α_Ω.

5.2.3) Evaluation of twisting

There are two ways to determine the twist angle from different kinds of rocking curve. The first and simplest way is to measure to the (10-11) Φ scan. The FWHM of the (10-11) Φ scan gives a direct value of the twist angle α_Φ. The second, more complex way to evaluate the twist angle is to measure a series of ω rocking curves with skew angle geometry. The twist angle is corresponding to the FWHM of ω rocking curve at an inclination angle of 90^o. However, direct measurement of ω rocking curve at an inclination of 90^o is geometrically impossible. Therefore, a series of ω rocking curve at several inclination angles as close as possible to 90^o are measured. In this study, (0002), (10-13), (10-12), (10-11) and (30-32) ω scan were performed. The FWHM values of these rocking curves can be plotted by the inclination angle. The FWHM value of reflection with

inclination angle of 90^{o} is extrapolated to the twist angle.

5.2.4) Estimation of dislocation density

Dislocation density can be estimated from the evaluated tilt angle and twist angle because the tilt and twist can be thought as a result of lattice distortion by screw and edge dislocation, respectively [5]. Dislocation density can be calculated by using formula of Ayers [6]. There have reports that successfully used to determine the dislocation densities in GaN epilayer. For screw dislocations the density, N_s can be expressed by such formula.

$$N_s = \frac{\alpha^2_{\varpi}}{4.35 b^2_s} \tag{1}$$

where b_s is the burgers vector of screw dislocation. α_{ω} is tilt angle. Meanwhile, in case of the edge dislocations, there are random and piled-up distributed dislocations. For randomly distributed edge dislocation density, N_e can be expressed by such formula.

$$N_e = \frac{\alpha^2_{\phi}}{4.35 b^2_e} \tag{2}$$

where b_e is the burgers vector of edge dislocation, α_{φ} is twist angle. For the screw dislocation density in hexagonal structure, the tilt angle and the burgers vector of <0001> are used, while for the edge dislocation density, the twist angle and the burgers vector of 1/3<11-20> are used.

5.2.5) Measurement of bowing curvature

Using the X-ray diffraction position, bowing curvature can be estimated. If the sample is bow in the plane along the c-axis, the incident angle (ω) of the X-ray with respect to the sample surface changes when the sample is moved along the distance(Δx). Then, the bowing curvature (R) of the sample can be estimated from the peak separation of diffraction curves ($\omega_2 - \omega_1$) with the distance (Δx) on the sample ($R = \Delta x \cdot (\omega_2 - \omega_1)$) [7]. Fig.5.2 shows schematically concaved surface of sample, whose diffraction angle increase as the sample in moved away from the X-ray source.

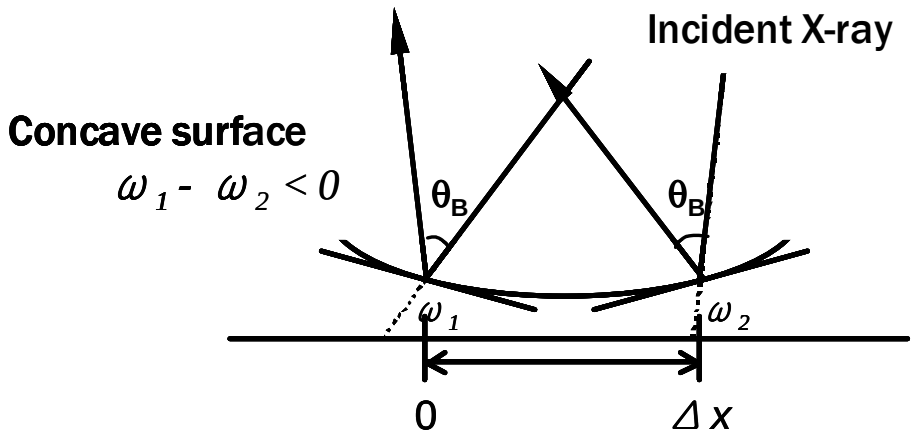

Fig.5.2. X-ray diffraction on concaved surface, which indicates bowing curvature

5.3) Specimen and Experimental procedures

Fig.5.3 shows schematic illustration of GaN substrate. Free-standing GaN substrates were grown on (0001) Al_2O_3 substrates by hydride vapor phase epitaxy (HVPE). We note that the thickness of the freestanding GaN substrates is very

thick (~ 2000 μm), which was naturally seperated from Al_2O_3 substrates. Then the front and back surfaces of the freestanding substrates were mechanically polished using diamond powders with 5 μm diameter.

The structural properties of the substrates were investigated by numerous ω scans for (0002) and (10-11) crystal planes using high-resolution X-ray diffractometer.(HRXRD) Also, surface damage is evaluated with increase of etching time stepwise. The KOH/ H_2O ratio of 1/4 as etching solution is employed. The GaN is observed every a day using PL, HRXRD and atomic force microscopy (AFM).

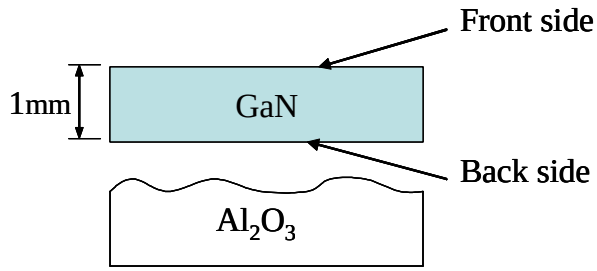

Fig.5.3. Schematic illustration of GaN substrate

5.4) Quantitative analysis of disorder in bulk GaN substrates

Fig.5.4 shows the Williamson-Hall plot of the sample, which roughly indicate tilt and twist angle for front side. Although the FWHM of (10-13) reflection shows the maximum values, we consider that the FWHM of (30-32) reflection is corresponds to twist angle in this study because an inclination angle of this reflection is close to 90^o.

Tilt angle for front side, which is corresponds to 0.048^o is nearly the same as

those of back side, which is corresponds to 0.049°. Meanwhile, twist angle for front side, which is 0.038° is broader than those of back side, which is 0.029°. This indicates that the reason for larger FWHM of front side may come from twisting rather than tilting.

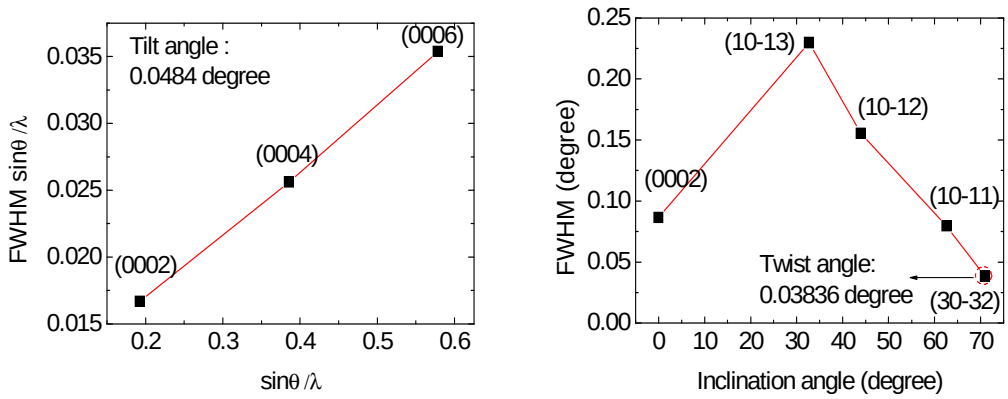

Fig.5.4 W-H plot for symmetric and asymmetric reflection using tilt/ twist angle

Then, dislocation densities for both faces can be estimated by Williamson-Hall plots, using a series of line width obtained with increasing the inclination angle of diffraction planes [5,8]. The front surfaces were estimated to have the screw and edge dislocation densities of ~ 6×10^{7} cm^{-2} and ~ 10×10^{7} cm^{-2}, respectively, while the back surfaces were characterized as to have the screw and edge dislocation densities of ~ 6×10^{7} cm^{-2} as listed Table 5.1.

Table.5.1 Screw and edge dislocations using W-H plot method.

	Tilt angle (degree)	Twist angle (degree)	Dislocation density evaluated by XRD	
			Screw dislocation (10^7 cm^{-2})	Edge dislocation (random) ($10^7 cm^{-2}$)
Front plane	0.0484	0.03836	6.090	10.11
Back plane	0.0497	0.0289	6.427	5.7361

5.5) Anisotropic broadening of XRC in GaN

Fig. 5.5 (a) and (b) show X-ray rocking curves for (0002) and (10-11) reflection of a free-standing GaN substrate. The X-ray rocking curves for (0002) reflection of front and back sides have a tail in (–) direction (low-angle side). Meanwhile, the asymmetric broadening is more clearly shown in the rocking curves for (10-11) reflection. Front side exhibits shoulders in (–) directions, while back side exhibits shoulders in (+) direction (high-angle side) shoulder respectively, as shown in Fig. 5.4(b). The inset shows rocking curve with log scale, respectively.

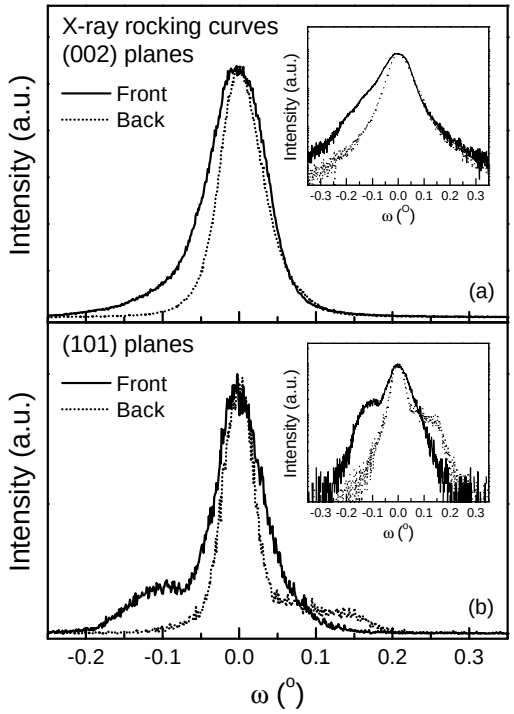

Fig.5.5 X-ray rocking curves for (a) (0002) reflection and (b) (10-11) reflection in GaN substrate. Solid line indicates front side and dotted line indicates back side

Fig.5.6 shows X-ray rocking curves for (0002) reflection of front side, obtained with decreasing the focusing area of incident beam by manipulating slit size. It is found that line shape becomes symmetric and line width becomes narrow with the decrease of the focusing area. The inset shows the focusing area dependence of line width for front and back sides.

It is found that the line width gradually decreases with the decrease of slit size. The asymmetric broadening and focusing area dependence of X-ray rocking curves are reported to be due to mosaic spreading of crystal planes or wafer bending

[3,9,10]. Yun et al. have found in free-standing GaN templates that X-ray rocking curves for (0002) and (10-14) planes are asymmetrically broadened and the rocking curves are changed with decreasing incident X-ray width [3]. The origin was attributed to the tilt and twist, which result in sub-millimeter scale mosaic spread.

On the other hand, Leszczynski et al. have reported that the broadening of X-ray rocking curves, obtained in GaN layers grown on Al_2O_3 substrates, is caused by a higher thermal expansion coefficient of Al_2O_3 with respect to GaN [11]. Kelly et al. have reported that the asymmetric broadening and focusing area dependence of X-ray rocking curves are induced by substrate bending, because the line shape and width were significantly changed after substrate lift-off [9].

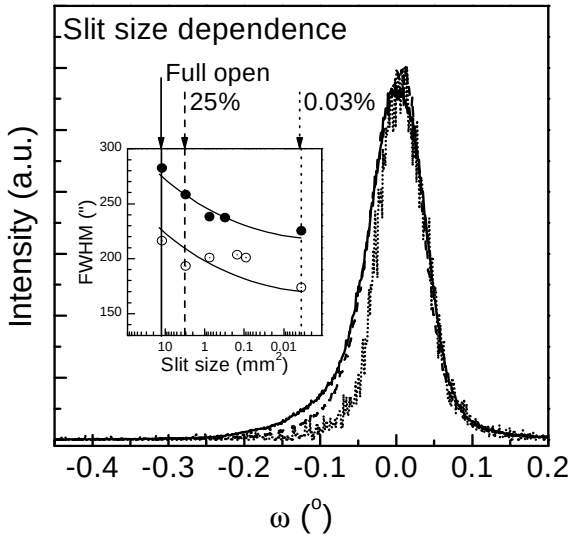

Fig.5.6. X-ray rocking curves for (0002) reflection of front side, obtained with decreasing the focusing area of incident beam by manipulating slit size. Inset shows the focusing area dependence of line width for front and back surfaces.

We have investigated the bowing curvature of free-standing substrates. It is found that the rocking curve for front surface shifts to higher angle side as the sample goes toward a diffractometer axis. The curvature is estimated to be –0.8 m, where the (–) sign indicates a concave surface. Moreover, it is found that the rocking curve for back surface shifts to lower angle side as the sample goes toward a diffractometer axis. Then the curvature is estimated to be +0.8 m, where the (+) sign indicates back surface has a convex curvature.

The results indicate that the free-standing GaN substrates suffer from substrate bowing to some degree. Similar results are available. Park et al. have reported that 2 inch free-standing substrates removed from Al_2O_3 substrates have a concave surface [10]. Kelly et al. have also reported about the bowing in free-standing GaN substrates in the opposite direction of the lift-off surface [9].

In this study, asymmetric broadening for (0002) reflection originates from tilt and surface bowing as shown in Fig.5.7(a). Also, the origin of asymmetric broadening for (10-11) reflection is mainly directional twist, which is rotated to the one direction as shown Fig. 5.7(b).

Grzegory et al. reported the rocking curve for symmetrical (002) reflection broadening reflects the presence of tilt mosaicity, and asymmetrical (220) reflection broadens which reflects the presence of twist mosaicity [12]. Consequently, it is expected that the anomalous behaviors found in X-ray rocking curves are ascribed to lattice deformation such as tilt, twist and substrate bowing.

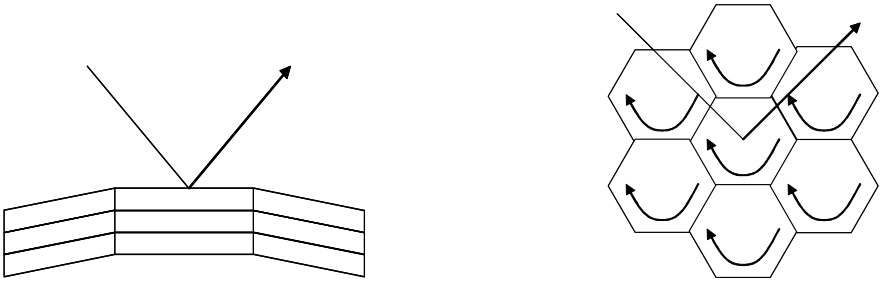

(a) (b)

Fig.5.7. Schematic illustration of (a) tilt and (b) directional twist structure, respectively

5.6) Evaluation of surface damage in GaN substrate

Fig.5.8 shows the reciprocal space mapping for (0002) reflection of front side. One can see that front plane has compressively strained surface layer. Campari et al report that surface damage in $LiNbO_3$ ion, exchanged in pure benzoic acid, originates mainly from a remarkably large strain, induced by the ion exchange between Li^+ and H^+ [13].

In this study, we consider that the surface damage such as the compressive strain is induced by an exchange of protons during the polishing such as Ga^+ and Al^+.

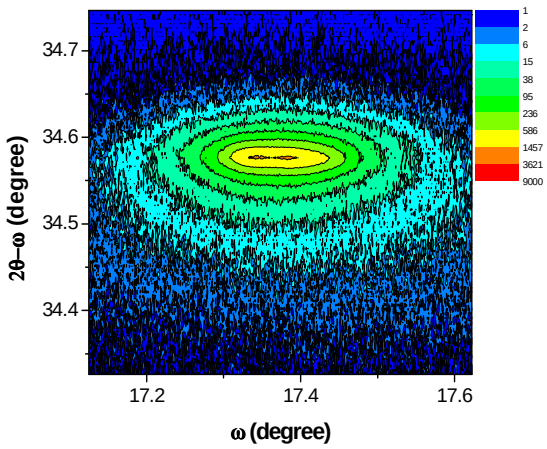

Fig.5.8. Reciprocal space mapping for (0002) reflection of GaN front side

To confirm the surface damage, GaN substrates were etched by KOH etchant and the structural and optical qualities of GaN were investigated. Fig.5.8 shows the surface morphology using atomic force microscopy (AFM). AFM along with appropriate techniques provides a convenient means to probe macroscopic structure and defects in GaN material.

Fig.5.9 (a), (b) is AFM surface image of front side with 10 μm range, while, Fig.5.9 (c), (d) is those of back side. After 96hr wet etching, front-side surface show a little increase of roughness from 11.2nm to 25.2 nm. While the back-side show large increase from from 13.7nm to 132.8nm.

This result directly indicates that front side is a Ga-polar surface and back side is a N-polar surface, since Grzegory et al. reports that Ga-polar surface is chemically inert, therefore it cannot be prepared by chemo-mechanical polishing [12].

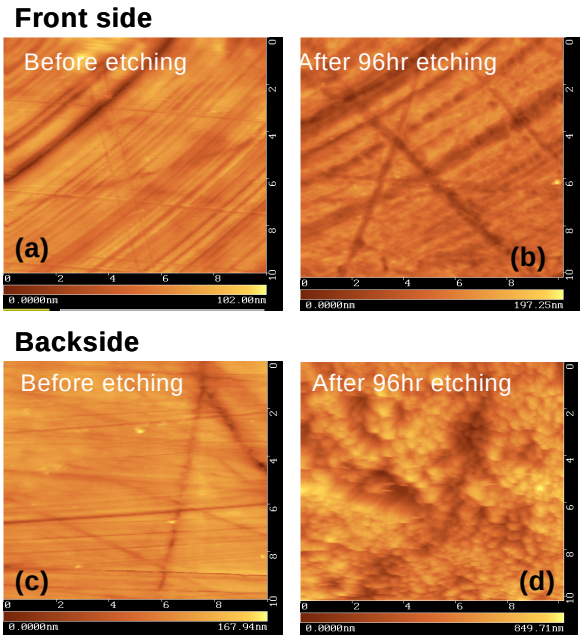

Fig.5.9. Surface image of unetched (a), (c) and 96hr etched (b), (d) GaN for front and back side

Fig.5.10 shows both the variation of surface roughness and XRD FWHM for (0002) reflection of front- and back-side with increase of etching time. Considerable variation of XRD FWHM is not observed for both sides. However, the surface roughness of back-side roughness increases as etching proceeds, while surface roughness of front side is not varied. It can be understood in terms of surface polarity.

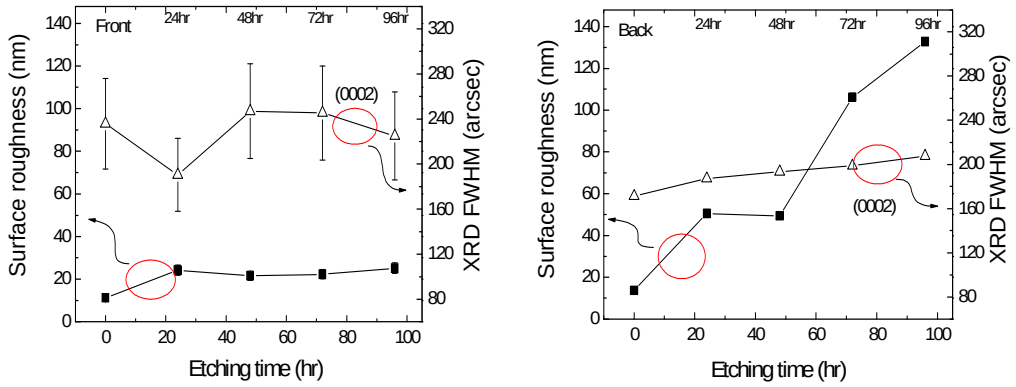

(a) (b)

Fig.5.10 Surface roughness and XRD FWHM of (a) front and (b) back side with etc hing

Fig.5.11 (a), (b) show PL spectra about front- and back-side of GaN substrate after 96hr etching at 300K, respectively. Two emission bands are observed. One is the edge emission band peak positioned at 3.39 eV, the other is the yellow band at 2.23 eV due to intrinsic defects related to nitrogen vacancy.

After the etching, strong UV emission intensity is observed from the front-side. The emission intensity ratio of the near band edge (NBE) emission to the yellow band emission increases about 2 times (I_{NBE}/ I_{YB} is changed from 3.2 to 6.8). Since the surface roughness does not show considerable increase, it is believed that the removal of surface damage layer elevates PL emission efficiency. Also, this result indicates that surface damage layer may be very thin.

On the contrary, as shown Fig 5.8 (b), in case of the back-side, the intensity ratio decrease about 2 times from 1.3 to 0.7. It is considered that large

deterioration of surface roughness affects the decrease PL intensity.

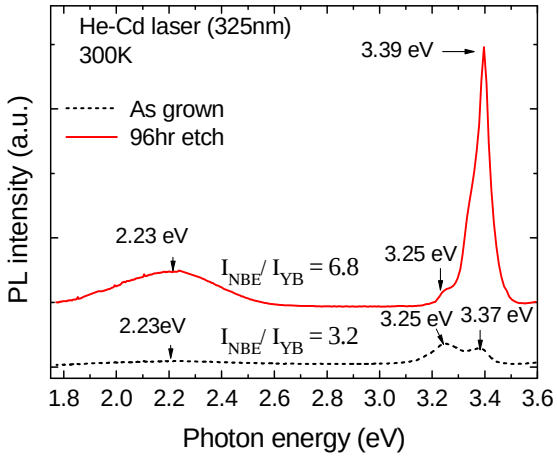

(a)

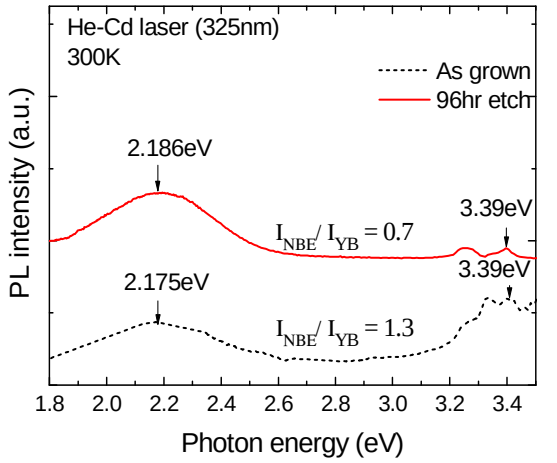

(b)

Fig.5.11. PL spectra about (a) front and (b) back side of unetched and 96 hr etched GaN substrate at 300K, respectively

5.7) Conclusion

In this chapter, we report on the lattice deformation found in free-standing GaN substrates grown by HVPE. Considerable asymmetric broadening of X-ray rocking curve for front and back surfaces is found, that can be ascribed in terms of the lattice disorders such as tilt, twist and bowing. This lattice disorder is evaluated using various HRXRD measurements. Also, it is discussed that the damage layers are originated by the polishing process by using chemical etching experiment. Consequently, the results indicate structural disorder can lead to serious defects such as surface damage.

Reference

[1] T. Detchprohm, K. Hiramatsu, K. Itoh, and I. Akasaki, Jpn. J. Appl. Phys. 31, L1454 (1992).

[2] K. Hiramatsu, T. Detchprohm, and I. Akasaki, Jpn. J. Appl. Phys. 32, 1528 (1993).

[3] F. Yun, M. A. Reshchikov, K. Jones, P. Visconti, H. Morkoc, S. S. Park, and K. Y. Lee, Solid-State Electron. 44, 2225 (2000)

[4] G. K. Williamson and W. H. Hall, Acta Metall. 1, 22(1953)

[5] T. Metzger, R. Hopler, E. Born, O. Abacher, Phil. Mag. A77, 1013(1998)

[6] J. E. Ayers. J. Crystal. Growth 135, 71 (1994)

[7] D. K. Bowen and B. K. Tanner, *High Resolution X-ray Diffractometry and Topography*, (Taylor & Francis Ltd, London, United Kingdom, 1998), p50.

[8] V. Srikant, J. S. Speck, and D. R. Clarke, J. Appl. Phys. 82, 4286 (1997)

[9] M. K. Kelly, R. P. Vaudo, V. M. Phanse, L. Gorgens, O. Ambacher, and M. Stutzmann, Jpn. J. Appl. Phys. 38, L217 (1999)

[10] S. S. Park, I. W. Park, and S. H. Choh, Jpn. J. Appl. Phys. 39, L1141 (2000)

[11] M. Leszczynski, T. Suski, H. Teisseyre, P. Perlin, I. Grzegory, J. Jun, S. Porowski, and T. D. Moustakas, J. Appl. Phys. 76, 4909 (1994)

[12] I.Grzegory, S.Porowski Thin Soild Films 367 (2000) 281-289

[13] *A. Campari, C. Ferrari, G. Mazzi J. Appl. Phys 58 (12)1985, 4521*

Chapter 6. Effect of structural disorder to electrical properties of GaN films

6.1) Introduction

Epitaxial films, which have a large lattice mismatch with their substrate, will have structural disorders such as mosaicity and bending. Also those structural disorders can affect the electrical properties of the film. Therefore, it is also important to investigate the defect in semiconductor device. Especially, defects have various effects on carrier transport mechanism as shown Fig.6.1 [1]. However, those are poorly understood and in most cases, it is very difficult to control experimentally, especially in case of GaN thin film [2].

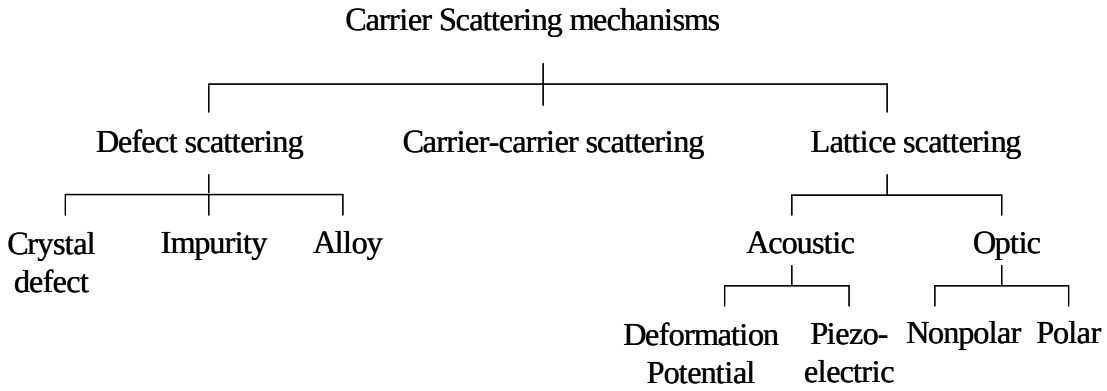

Fig.6.1. An outline of the possible carrier scattering mechanisms

In this chapter, electrical properties of disordered semiconductors have been investigated. Hall measurements were performed on GaN film grown on the (0001)

Al_2O_3 substrate by HVPE. The experimental data is analyzed in terms of the conduction through defects. Also a model is proposed to explain the observed extremely low mobility in the films.

6.2) Experimental

In this chapter, GaN thin film with thickness of ~ 250 μm has grown on (0001) Al_2O_3 substrate using HVPE. Prior to the growth of GaN epilayer, AlN with thickness of about 80nm has grown by metalorganic hydride vapor phase epitaxy (MO-HVPE). The growth rate of MO-HVPE system was about 250 μm/hr. Trimethyl Aluminum was used as an Al source and growth temperature for AlN buffer was 900℃, although the growth condition for AlN buffer layer is not optimized yet. To evaluate lattice disorders, GaN thin film were investigated by atomic force microscopy (AFM), X-ray diffraction (XRD) and temperature dependent Hall effect measurement from 10K to 300K. For the electrical measurements, Ohmic contact was made by Al, which was evaporated by thermal evaporator and deoxidized for 10min at at 560℃. Fig.6.2 shows the schematic illustration of GaN thin film using AlN buffer layer.

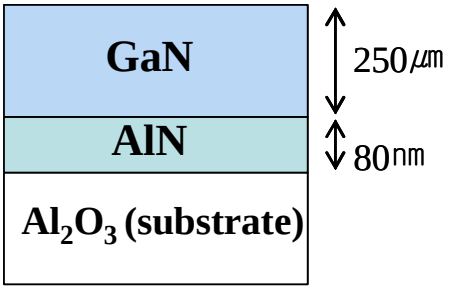

Fig.6.2. Schematic illustration of GaN film using AlN buffer

6.3) Morphological and structural characterization of GaN thin film

Fig.6.3 shows the AFM image of GaN film using AlN buffer. From AFM image, surface roughness of GaN film is found to be 2.3 nm.

Although several pits are observed because the growth condition for AlN buffer layer is not optimized yet, GaN epilayer has similar surface roughness in compared to GaN film without AlN buffer layers.

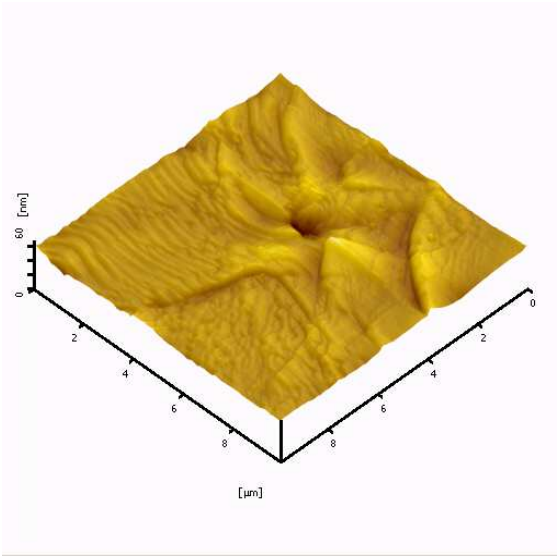

Fig.6.3. AFM image of GaN film using AlN buffer

High resolution X-ray diffraction (HRXRD) is performed for GaN film to investigate the structural qualities. Fig.6.4 show the (a) ω-2θ scan and (b) ω scan for (0002)/(10-11) reflection of GaN thin film. For (0002) reflection, the FWHM of ω-2θ is about 63 arcsec, and the (10-11) reflection has FWHM of 114 arcsec. Also, the rocking curve of ω scan for (0002) reflection is 1209 acrsec, and for (10-11) reflection is 2299 arcsec.

Generally speaking, the FWHM of ω-2θ indicates the residual strain and disorder in reflection planes, while the linewidth of ω rocking curve informs crystal mosaicity [3]. Because dislocations of both [0001] and [10-10] two directions in case of (10-11) reflection affect in GaN thin film, the FWHM of (10-11) reflection is about 2 times broader than those of (0002) reflection. Therefore, the ω-2θ scan for (0002) and (10-11) reflection indicates surface normal and in-plane directional lattice disorders, respectively. These disorders will affect the dislocation density in the film also electrical properties.

Edge dislocation of 2.9×10^{9} cm^{-2} and screw dislocation of 2.7×10^{10} cm^{-2} is estimated by using W-H plots method, which has been introduced in chapter. 5. This result shows the existence of large number of dislocations within GaN film.

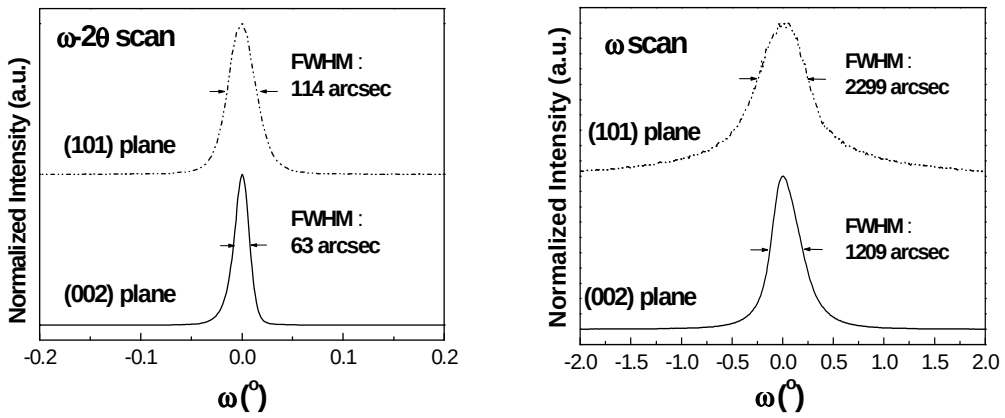

(a) (b)

Fig.6.4 (a) ω-2θscan and (b) ω scan for (0002) and (10-11) reflection of GaN thin film.

6.4) Electrical characterization of GaN thin film

In this part, the electrical properties of GaN film with high dislocation density will be discussed. Electrical contact was formed by thermal evaporation using Aluminum and Ohmic contact was confirmed by linearity of I-V curve. The magnetic field used for Hall effect measurement was 3500 gauss.

Fig.6.5 shows the mobility of GaN at the elevating temperature from 10K to 300K. The maximum value of electron mobility is about 20$cm^2/V \cdot S$ at 200K. The result shows that mobility increases until 200K, then decreases as the measurement temperature increase. There are reports that GaN films produced by a variety of deposition methods were generally found to have low electron mobility. Ilegems et al report that the epitaxial growth of GaN with 100–200 μm thick were obtained on (0001) Al_2O_3 substrates by Hydride vapor phasel epitaxy (HVPE), which have carrier concentrations of 1–2 $\times 10^{17}$ cm^{-3} with electron mobilities near 400 cm^2/V sec at 300 K [4]. On the other hand, Nakamura report GaN film grown by Metalorganic chemical vapor deposition (MOCVD) has the mobility of 900 cm^2/V sec and carrier concentration of ~3 $\times 10^{16}$ cm^{-3} [5].

In general, temperature dependent mobility can be explained in terms of phonon scattering and ionized impurity scattering [6]. The mobility increase as temperature decreases because thermal lattice fluctuation has effect on carrier transportation. While, although lattice fluctuation incompletely occur at low temperature, mobility decrease due to ionized impurity scattering. The whole mobility is expressed by following formula, coupling with two scattering.

$$1/\mu = 1/\mu_{ion} + 1/\mu_{lat} \quad (1)$$

where, μ_{ion} is the mobility due to the ionized impurity scattering, μ_{lat} is the mobility due to lattice scattering. Theoretical temperature dependence should have well known dependence of temperature such as lattice scattering ($T^{-3/2}$) and impurity scattering ($T^{3/2}$). However, it is found that the measured mobility is proportional to $T^{-1/50}$ above 200K and $T^{1/5}$ below 200K. The observed T-dependency indicates an existence of additional scattering mechanism.

Look suggested that defect scattering, including crystal defect, impurity and alloy is closely relate to carrier scattering of practical crystal [1]. It is considered that in case of GaN film with high dislocation density, carrier scattering at dislocations may lower the mobility [1].

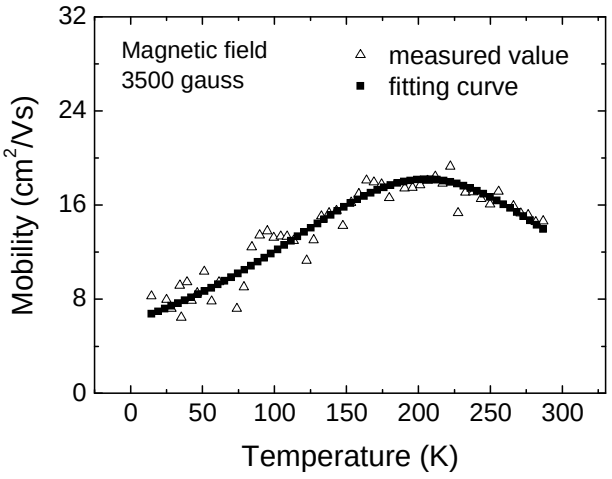

Fig.6.5 T-dependent carrier mobility

Also, low mobility can be explained by using the potential barrier model, which is suggested by Shalish et al [7]. Assuming that a potential barrier and small applied bias, which is effective bias much smaller than the thermal voltage across each grain, barrier-limited transport is characterized by an exponential dependence of the conductivity, σ, on the average grain boundary barrier height Φ_{gb}.

$$\sigma = \sigma_0 \exp(-q\Phi_{gb}/kT) \quad (2)$$

where σ_0 is a proportionality coefficient, q is the electron charge, k is the Boltzmann constant and T is the temperature. Fig.6.6 shows the variation of conductivity (ln σ) with reverse temperature (1000/T). From the Fig.6.3, Φ_{gb} is estimated to about 34.9 meV, which indicates height of potential barrier.

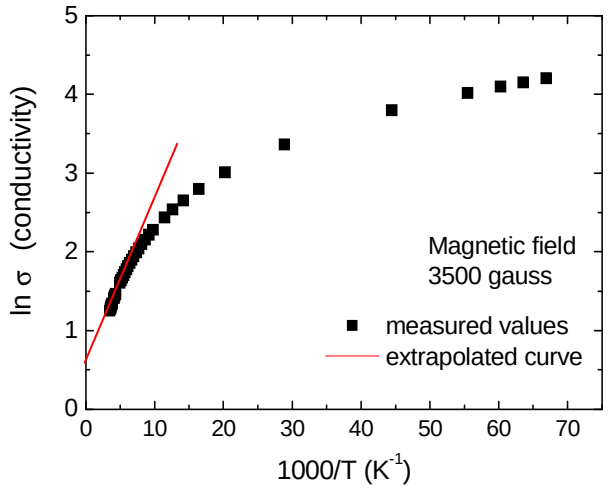

Fig.6.6 Measured value of conductivity (ln σ) versus reverse temperature (1000/T)

Such a potential barrier is known as to be formed. It should be noted that low mobility due to the potential barriers in a crystal describes a sample with high dislocation density. In this experiment, the GaN film has high dislocation density as shown in XRD result. Therefore, the low carrier mobility is attributed to the high dislocation density in the GaN film. High dislocation density strongly influence on the carrier transportation, which is almost occurred at a grain boundary as shown in Fig.6.7 [7].

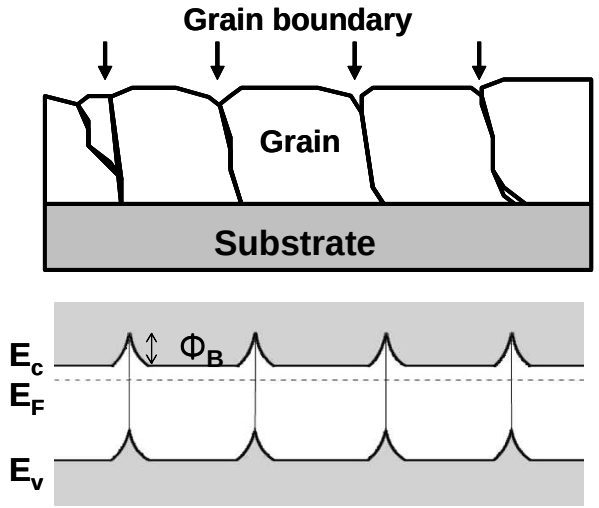

Fig.6.7 A schematic diagram of a film possessing a columnar grain structure and equilibrium band diagram.

The potential barrier model is useful to understand relationship between dislocation and carrier transportation directly. Fehrer and Herzee report that grain boundary restricts the electron mobility by band bending [8,10]. Since the grain are single crystalline domain surrounded by dislocation. High density dislocations make small grain size, which results in high density potential barriers. Thus, it is

considered that mosaicity creating this potential barrier in GaN lead to low mobility.

Fig.6.8. shows the carrier concentration of GaN at the elevating temperature (10K to 300K). The unintentionally doped GaN show n-type conductivity with the carrier concentration of 3×10^{18} cm^{-3} at room temperature and 7×10^{18} cm^{-3} at 13K. At high temperature region (200K~300K), the carrier concentration is almost constant, while, it increases (50K~200K) then decreases again until 10K.

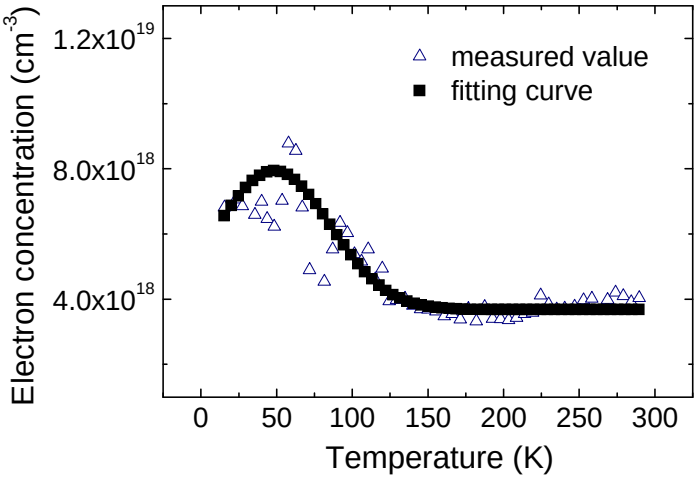

Fig.6.8. T-dependent carrier concentration

Temperature dependent carrier concentration is theoretically expressed by following formula [9].

$$n(T) = n_0 \exp\left(-\frac{E_n}{kT}\right) \tag{3}$$

Where, E_n is the activation energy of carrier, n_o is proportionality coefficient.

The activation energy of carrier can be approximately estimated using the formula (3).

Fig.6.8 shows that the carrier concentration is fitted in the reverse temperature (1000/T) of range from 200 to 300K, and the inset also shows the ln(N) in according to the variation of each reverse temperature ranges; 13-70K and 200-300K, respectively, which informs the activation energy. Using the formula (2), the activation energy of 5.7 meV and 32.6 meV are estimated at the temperature of 13-70 K and 200-300 K, respectively.

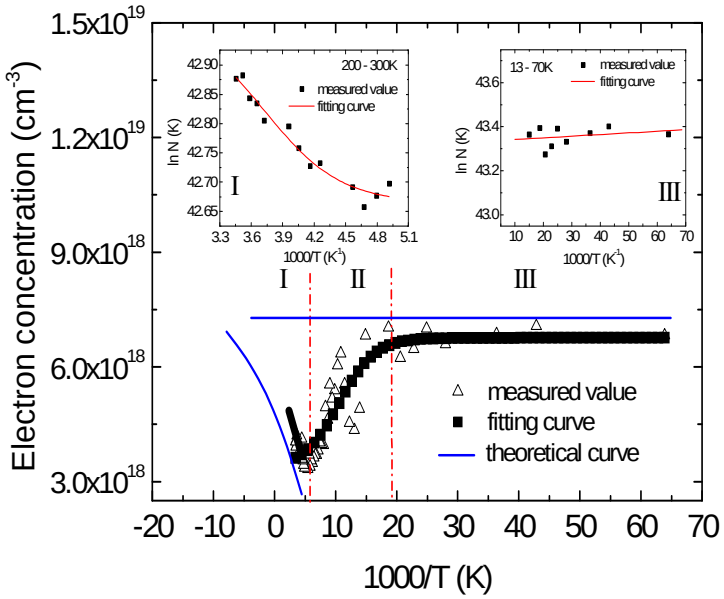

Fig.6.8 the fitting curve of carrier concentration

It can be explained that at low temperature below 50K, donor in conduction band freeze out and conduction via defect level is dominate because of Fermi level

pinned by the defect. Therefore, the variation of carrier concentration is not observed. While, at higher temperatures, electrons at donor level will be activated and dominate the carrier concentration, which brings the carrier concentration variation.

Molnar et al. reported that the measurements at high temperatures were dominated by the conduction band electrons, while defect band become dominant when carriers in the conduction band become negligible at low temperature [2].

At lower temperatures, the increase of carrier concentration is related to the defects, corresponding to high dislocation density at grain boundary in GaN thin film. If the concentration of donors is smaller than the deep defects known to exist in GaN film, the material will be fully compensated with its Fermi level pinned by these defects. In such a material, transport is dominated by hopping in the compensating centers leading to low electron mobilities [2].

6.5) Conclusion

In this chapter, structural disorder and related electrical properties were discussed. Electronic properties of GaN film are investigated by using T-dependent Hall effect measurements in terms of carrier transportation. Structural properties such as dislocation density are estimated using HRXRD measurement. Consequently, it is found that high dislocation density is related to low carrier mobility. Defect and dislocation induced structural disorder including mosaicity is found to be an origin of poor electron transportation.

Reference

[1] David C. Look, *Electrical characterization of GaAs materials and devices*, John Wiley & Sons, p74.

[2] R.J. Molnar, T. Lei, and T. D. Moustakas , Appl, Phys. Lett. 62(1)72

[3] Q.Zhu, A.Botchkarev et al, Appl. Phys. Lett. 68, 1141 (1996)

[4] M. Ilegems, J. Cryst. Growth 13/14, 360 (1972)

[5] S. Nakamura, T. Mukai and M. Senoh, J. Appl. Phys 71 (1992) 5543

[6] Seong-Il Kim, Chang-Sik Son et al, Solid State Comunications Vol.93, No11, pp.939-942, 1995

[7] I. Shalish, L. Kronik , G. Segal et al, Phys. Rev. B 61, 15573 (2000)

[8] M.Fehrer, S.Einfeldt, U.Birkle et al, Journal of Crys. Growth 189/190 (1998) 763

[9] D. K. Gaskill, L. B. Rowland, and Doverspike, properties of group III nitrides, INSPEC, London, 1994, chap 3

[10] S. D. Herzee, J. C. Ramer, Material. Res. Bull. 22 (1997)

Chapter 7. Summary and conclusion

The study of crystalline materials has played a prominent role in the traditional approach to solid state physics. In general, many practical applications use materials that are disordered because there are several problems such as lattice deformation, surface damage, interface roughness and uniformity of composition and so on. These disorders induce the deterioration of device quality. In order to confirm the origins which determine degradation of device, it is necessary to investigate several disorders, also, to control and reduce the disorders in semiconductors due to improve the semiconductor device performance up to theoretical limits. In this work, we not only evaluated several disorders, interface disorder, composition disorder in QWs, lattice disorder including mosaicity, tilt, twist in bulk, epil-layer material by using various methods such as PL, HRXRD and Hall measurements, but also considered how to lower up to theoretical values this disorder, which affect in semiconductor device.

We expect that those studies about disorder become standard guilds, evaluating the crystallinity of hetero-structures, bulk materials and thin films.

In the first chapter, various disorders such as structural, orientational, compositional and vibrational disorder in compound semiconductor are introduced. Also, the origins of such disorders have been discussed in terms of various physical properties such as optical, electrical, structural properties. The importance of this

study is considered to control and reduce the disorders in semiconductors due to improve the semiconductor device performance up to theoretical limits.

In the second chapter, the principles and used equipments of three methods to evaluate the disorders effect was introduced in terms of structural, optical and electrical properties.

In the third chapter, $Zn_{1-x}Cd_xSe$/ZnSe TQW is grown by using MBE and investigated in terms of PL linewidth. In case of composition disorder, the measured and calculated PL linewidth show agreement when the Cd-composition is low. However, disagreement increases as Cd-composition increase due to Zn/Cd inter-diffusion.

In the fourth chapter, $Zn_{1-x}Cd_xTe$/ZnTe MQW is also grown by using MBE and evaluated using PL linewidth as well as high resolution X-ray rocking curve. High quality ZnCdTe QWs are controlled by using RHEED intensity oscillation. When QW thickness is considerably smaller than Bohr radius of exciton, PL line width has much smaller value in compare with experimental result. However, if the QW thickness is similar or larger than exciton radius, the experimental results show considerable agreement with the calculated values.

In the fifth chapter, structural qualities of freestanding GaN substrate (~1mm) grown by HVPE are investigated using HRXRD measurement. X-ray rocking curve of front plane is asymmetrically broadened because of lattice disorders such as tilt, twist and substrate bowing, which can be confirmed from silt size dependence, calculation of bowing curvature. Also, the surface damage layers

originated from polishing is not only observed using AFM image, PL spectra, but also tried to remove using chemical etching.

In the last chapter, GaN thin film (~250 μm) grown by HVPE using AlN buffer layer is investigated using T-dependent Hall effect measurement, HRXRD. Considerably low mobility and high dislocation density is observed. It is considered that high dislocation density is related to low carrier mobility. Defect and dislocation induced structural disorder such as mosaicity are explained in terms of `potential barrier`. Consequently, it is found that structural disorder strongly affect on electrical transportation.

Appendix A

1. Transition energy of ZnTe QW

The transition energy of ZnTe QW can be expressed by the following formula (A.2). E_g is bandgap of unstrained quantum well, E_b is the binding energy due to Columb attraction [1] E_s is energy shift due to lattice misfit. E_{stokes} is energy shift due to inhomogeneous interface. E_{elec} and E_{hole} is energy due to quantum effect in case of n=1.

$$E_{QW} = E_g + E_{elec} + E_{hole} - E_b \pm E_s - E_{stokes} \quad \text{(A.2)}$$

In case of ZnTe QW with variation of Cd-composition, x, E_g is calculated using following formula (A.3),

$$E_g\,(Cd_xZn_{1-x}Te) = 1.606x+2.394(1-x)-0.26x(1-x) \quad \text{(A.3)}$$

The energy of quantum state is calculated using following formula (A.4). [1] In case of ZnTe, effective mass of hole is $0.54m_0$ (heavy hole), effective mass of electron is $0.12m_0$

$$E_1 = 3.76\left(\frac{m_0}{m}\right)\left(\frac{10nm}{L}\right)^2 \ \text{(meV)} \quad \text{(A.4)}$$

The ZnCdTe QW is compressively strained because of lattice mismatch with ZnTe substrate., which lead to variation of energy band structure as shown in Fig.

A.1. ΔV_c is the energy shift of conduction band. ΔV_{hh} and ΔV_{lh} is the energy shift of valence band due to split between heavy hole and light hole respectively, which can be expressed by following formula (A.5).[2] E_g^* is energy gap as compressive strained ZnTe. ε is horizontal component of strain. C_{ij} is stiffness coefficient, a_c and a_v is conduction and valence band hydrostatic deformation potential, respectively. b is the valence band shear deformation potential. When $Cd_{0.2}Zn_{0.8}Te$ QW is grown on ZnTe, E_g^* increase about 14.5meV due to compressive strain.

$$\begin{aligned}
\Delta V_c &= 2a_c \frac{C_{11}-C_{12}}{C11}\varepsilon \\
\Delta V_{hh} &= -2a_v \frac{C_{11}-C_{12}}{C11}\varepsilon + b\frac{C_{11}+2C_{12}}{C_{11}}\varepsilon \\
\Delta V_{lh} &= -2a_v \frac{C_{11}-C_{12}}{C11}\varepsilon - b\frac{C_{11}+2C_{12}}{C_{11}}\varepsilon
\end{aligned} \qquad \text{(A.5)}$$

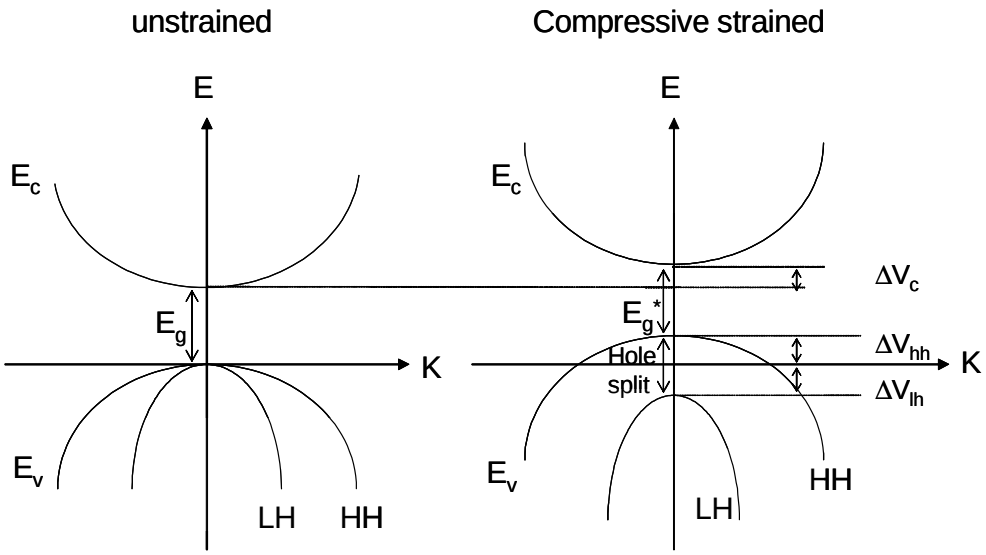

Fig.A.1 The variation of energy band structure due compressive strain

2. Material constant of ZnTe used for calculation of this work [3].

Material constant	ZnTe
Crystal Structure	Zincblende
Lattice constant (Å)	6.101
Energy gap at 0K (eV)	2.39
Electron mass (m_0)	0.12
Heavy hole mass (m_0)	0.54
Light hole mass (m_0)	0.13
C_{11} (10^{11} dyn/cm^2)	7.13
C_{12} (10^{11} dyn/cm^2)	4.07
a_c(eV) [4]	-3.653
a_v (eV) [4]	1.827
b (eV)	-0.92
Exciton binding energy (meV)	13.2

[1] L. A. Coldren, S. W. Corzine, *Diode lasers and photonic integrated circuits*, John wiley & Sons, Inc. p396

[2] C. M. Wolfe, N. Holonyak Jr and G. E. Stillman, *Physical properties of semiconductor*, Prentice Hall (1989)

[3] Landolt-Bornstein, New series Group Ⅲ, vol.17, Springer (1982)

[4] C. G. Van de Walle, phys. Rev. B, 39 (1989)

Appendix B

1. Calculation of interface disorder of ZnCdTe

$$\gamma_{\text{int}} = \sqrt{2}\,\frac{\delta_2}{\rho_{ex}}\left(1.4\sqrt{C_a^0 C_b^0}\right)\left(C_a^0\Delta^+ + C_b^0\Delta^-\right)$$

$$\Delta^+ = \left.\frac{\partial E_{ex}}{\partial L}\right|_{L_0+\delta L}\cdot\delta_1 \qquad \Delta^- = \left.\frac{\partial E_{ex}}{\partial L}\right|_{L_0-\delta L}\cdot\delta_1$$

δ1: The height of CdZnTe island; 0.15nm δ_2 : Diameter of CdZnTe island; 5nm

L_0 : Thickness of quantum wells

ρ_{ex} : The lateral extent of the exciton wave function; exciton radius of ZnTe= 5.5nm, ZnSe=4nm

C_a+C_b = 1 (normalization)

2. Calculation of composition disorder of ZnCdTe

$$\gamma_{all} = 2\sqrt{\frac{V_c}{V_{ex}}1.4x_0(1-x_0)(1-P_{ex})}\Delta_1$$

V_c : the volume per anion site ; r_0^3=0.198nm

V_{ex} : a critical volume of exciton ; Exciton radius of ZnTe= 5.5nm, ZnSe=4nm

X_0: Cd-composition in ZnCdTe QW

P_{ex}: the probability for the exciton to penetrate into the well barrier, only the fraction (1-P_{ex}) of the exciton is confined in the well.

$$\frac{1}{17.7245}\int_{-x}^{x}\exp(-0.4x^2/40) \qquad \text{(normalization)}$$

Acknowledgements

I greatly thank in my heart to Professor Jiho Chang for his continuous guidance, encouragement and supervision during this work. His coaching helps me not only to set a goal for this thesis but also to support my life during the master's course. I would like to thank to Professor Samnyung Yi, Hyungsu Ahn, Min Yang and Hongseung Kim for their critical comments and advise on this work.

In the course of this work, many people have assisted me in Tohoku university. I greatly thank to Prof. Takafumi Yao and Prof. Meoungwhan Cho for giving an opportunity to study as a research student during six months in Japan. I especially thank to Dr. Dongcheol Oh, Dr. Jungjin Kim and Mr. Wookhyun Lee for giving me many important suggestions for my thesis and supporting my living in Japan. I also would like to thank to Dr. Inho Im, Prof. Hyunchul Ko and Mr. Seogwoo Lee, Mr. Sanghyun Lee for various assistances during my staying in Japan. I thank to Dr. Takashi Hanada and Prof. Hisao Makino for his valuable advice. I am grateful to Takahiro Mori, Tsutomu Minegishi, Hideyuki Suzuki, Hiroki Goto, Backmater Ryan, Baba Takeshi and Miss. Zahara Vashaei for the assistance in experiment, as a friend and as a coworker.

I would like to thank to Kyunghwa Kim, Hyang Kim, Jungyeoun Yi and Juyoung Lee for the helps in the beginning of my master's course.

I should also thank to Myunghun Jung for the discussions on MBE growth as my coworker and friend, and Mina Jung, Kwanghee Kim, Sunyue Ha and Jinwoo

Jung for the assistance and reinforcement as a junior student in my laboratory. I also thank to Daehyun Shin, Hojun Lee, Eunsu Jung and Kunsuk Jang for their helps during my master degree period. I wish their achievements and progress through their master degree course. Also, I really appreciate to my best friend, Changhwan Ahn, for the spiritual encouragement in my life as a fellow student.

Finally, I am grateful to my lovely parents for not only giving birth to me but also caring me so far. Their love and trust really becomes strong support for me. I never forget this gratitude for them, forever.